Supporting Information for

"Continent-side paleo-rift structure in the western East Sea (Sea of Japan) and linkage between Moho uplift and mountain range formation"

Jeongin Lee[1], Tae-Kyung Hong[1*], Junhyung Lee[1], Seongjun Park[1], Byeongwoo Kim[1], Samuel Celis[1], and Yanbing Liu[1]

Affiliation and address:

[1]Yonsei University, Department of Earth System Sciences, 50 Yonsei-ro, Seodaemun-gu Seoul 03722, South Korea.

Correspondence to:

tkhong@yonsei.ac.kr (Tae-Kyung Hong)

Contents of this file

Introduction

This supporting information provides additional information and data on the method, process, and results.

Method

We apply a time-domain iterative deconvolution method to search for the optimal receiver function that minimizes the misfit error between the observed radial seismograms and synthetic receiver functions formed by convolving vertical P waves (Kikuchi and Kanamori, 1982; Ligorria and Ammon, 1999). We apply a Gaussian filter to the waveform using Gaussian bandwidth constant (α) of 1.0, 2.5. The Gaussian filter is given by

$$H(f) = \exp\left[-\left(\frac{\pi f}{\alpha}\right)^2\right], \tag{S1}$$

where f is the frequency.

We calculate the time lags of radial wavetrain spikes by cross-correlating with the vertical P waveforms (Ligorria and Ammon, 1999):

$$r_h(t') = \int_0^\infty z(t)\, h(t+t')\, dt, \tag{S2}$$

Where $r_h(t)$ is the cross-correlation function, $z(t)$ represents the observed vertical P waveforms, and $h(t)$ represents the observed radial waveforms at time t. The amplitude of spike is calculated by

$$R_a(t) = \frac{r_h(t)}{r_z(t)}, \tag{S3}$$

Where $R_a(t)$ represents the amplitude of the receiver function and $r_z(t)$ is the autocorrelation function of vertical P waveforms at time t.

We calculate synthetic radial waveforms by superposing the vertical P waveforms (Kikuchi and Kanamori, 1982; Wang and Pavlis, 2016):

$$y(t) = \sum_{l=1}^{N_s} R_a(t_l) \ \{z(t) * \delta(t - t_l)\}, \tag{S4}$$

where $y(t)$ is the synthetic radial waveforms at time t, N_s is the number of spikes, $z(t)$ is the vertical P waveforms, and t_l is the lag time of lth spike. We iteratively search for the optimal number of spikes until the misfit error is sufficiently low between synthetic observed and radial waveforms. The misfit error is calculated by

$$\Delta_h = \int_0^\infty [h(t) - y(t)]^2 dt, \tag{S5}$$

where $h(t)$ is the observed radial waveforms, and $y(t)$ is the synthetic radial waveforms at time t.

In order to find the optimum set of damping factor and influence factor, we examine the accuracy of the inverted velocity models using a synthetic test. We estimate the root mean squares errors (RMSEs) between input model and inverted model:

$$\mathrm{RMSE} = \sqrt{\frac{1}{N} \sum_{i=1}^{N} \left(v_i^I - v_i^T\right)^2}, \tag{S6}$$

where N is the number of layers in the velocity model, v_i^I is the inverted velocity in layer i, and v_i^T is the true velocity in layer i. We measure the model deviation (R_1) and model roughness (R_2) of inverted velocity model:

$$\begin{aligned} R_1 &= \sqrt{\frac{1}{N-1} \sum_{i=1}^{N-1} \left(v_{i+1}^I - v_i^I\right)^2}, \\ R_2 &= \sqrt{\frac{1}{N-2} \sum_{i=1}^{N-2} \left[(v_{i+2}^I - v_{i+1}^I) - (v_{i+1}^I - v_i^I)\right]^2}. \end{aligned} \tag{S7}$$

The model deviation and model roughness assess the differential velocity change across the layers, presenting the smoothness of the velocity model.

Additional information on data process

We analyze seismic records of 109 stations in the eastern Korean Peninsula (Fig. S1). We collect Rayleigh-wave dispersion data in periods of 1-15 s from a ambient-noise tomography study (Park and Hong, 2024). We calculate the surface-wave (Rayleigh, and Love waves) dispersion data in periods of 15-60 s from an analysis of 13 local seismic events (Table S1).

We analyze 119 teleseismic earthquakes with magnitudes $\geq M_W 6$ that occurred in January 2019 to January 2024 for receiver function analysis (Table S2). The numbers of teleseismic events analyzed in each station are 19-104. The events are distributed over wide back azimuths of 30°-50°, 120°-225°, and 300°-315° (Figs. S2, S3).

We determine vertical S-wave velocity models for the media beneath stations using an iterative least-squares inversion method. We perform a joint inversion with an influence factor of $\gamma = 0.15$ and a damping factor of $\eta = 0.5$ (Fig. S4). There is a low-velocity layer observed at 3 to 6 km depth. A velocity jump is visible at 30 to 35 km, which is the Moho. We determine the crustal thickness and V_P/V_S ratios using an $H - \kappa$ stacking analysis. We stack receiver function amplitudes of three Moho-converted phases (Ps, $PpPs$, $PsPs$+$PpSs$). Moho-converted phases arrival time is calculated considering slowness. Receiver function with Gaussian filter parameter of $\alpha = 1.0$ as a function of ray parameter (Fig. S5). The observed receiver functions agree with the theoretical arrival times of Moho-converted phases. We search an optimal set of crustal thickness and V_P/V_S ratio that maximizes $s(H, \kappa)$ (Fig. S6). The crustal thickness and V_P/V_S ratios beneath stations are presented in Table S3.

We interpolate the 1-D shear-wave velocity models for media beneath stations, obtaining 3-D shear-wave velocity models of the study region (Fig. S7). Also, the differential shear-wave velocities relative to the average shear-wave velocities are estimated (Fig. S8). For crustal thicknesses in offshore region, we consider a crustal velocity model, CRUST1.0 (Laske et al., 2013). The crustal thicknesses along profiles MM', NN', and OO' gradually decrease toward the east to approximately 25 km in the East Sea (Fig. S9).

We compare the Bouguer gravity anomalies with crustal thicknesses (Fig. S10(a)). We estimate the average Bouguer gravity anomaly at every crustal thickness. We find an apparent linear relationship between the Bouguer gravity anomalies with crustal thicknesses. Similarly, we compare the heat flows with crustal thicknesses (Fig. S10(b)). We find a mild inverse

correlation between heat flows and crustal thicknesses. Thin crustal regions (22-26 km) present relatively high heat flows.

The seismicity is high around the paleo-rift structures off the eastern Korean Peninsula. The focal depths in the offshore regions are 5-35 km (mostly in 15-20 km), while those in inland regions are 5-25 km (mostly in 5-10 km) (Fig. S11). The focal depths in offshore regions are deeper due to the earthquake occurrence in the paleo-rift structures that extend across the crust.

Offshore-station analysis

We analyze the records from two permanent island stations (DOKDO and ULDR) and two ocean bottom seismometer (OBS) stations (E208 and E209) to investigate the offshore crustal structure and its relationship to inland crustal deformation (Fig. S12). The offshore structures may provide insights into the connection between continental rift and inland crustal structures. The OBS stations are located in the boundary between Hupo bank and Ulleung basin that may be close to the rift center (Lee et al., 1999). On the other hand, the island stations (DOKDO and ULDR) are located in Ulleung basin.

The OBSs were deployed by free fall. Thus, the OBS sensors are oriented in arbitrary directions (Hung et al., 2019). Also, a thick sediment layer and a water layer may contribute to anisotropic effects (Wang et al., 2020; Yang et al., 2023; Gong et al., 2024). Before we conduct the receiver function analysis (Herrmann, 2013), we first determine the true sensor orientations (Park and Hong, 2024). We find that the true sensor orientations are 353.1° for E208 and 47.9° for E209 from the nominal directions. The OBS stations were operated continuously for 6 months to 1 year before being redeployed. We collect 37 teleseismic events during the operational periods (Table S4). Eight event records are removed due to their unclear P arrivals. The backazimuths of events range between 120° and 230° (Fig. S13).

Notably, the amplitudes of the P-to-S converted phases in the receiver functions present apparent variations with backazimuth. This feature may be caused due to lateral variation in crustal structures. The abrupt transition in crustal structures in the continental shelf margin between the Hupo bank and Ulleung basin may affect the seismic waveforms (Kim et al., 2003; Lee et al., 2015).

Receiver function amplitudes from three Moho-converted phases (*Ps*, *PpPs*, *PsPs+PpSs*) are stacked using weights $\omega_1 = 0.7$, $\omega_2 = 0.2$, and $\omega_3 = 0.1$ (Fig. S14). The receiver functions recorded at offshore stations present high azimuthal and slowness-dependent variation, suggesting strong lateral heterogeneity or anisotropy in the media. These complexities likely reduce the coherency of Moho-converted phases in the stacking process, resulting in ambiguous or trade-off-driven solutions.

A constant average crustal *P*-wave velocity of 6.0 km/s is assumed, based on the CRUST1.0 (Laske et al., 2013). We perform a forward inversion of receiver functions using a half-space initial model based on the offshore crustal structure from CRUST1.0 (Laske et al., 2013). The velocity models beneath island stations are inverted relatively stable, while those beneath OBS stations are unstable. The unstable inversion for OBS stations may be partly due to ocean noise and poor determination of sensor orientation. We finally present the velocity model for stations ULDR, DOKDO and E208 (Fig. S15).

The velocity models inverted from receiver functions reveal shear-wave velocity increases at depths that are consistent with the crustal velocity model (CRUST1.0). Island stations ULDR and DOKDO present velocity jumps at depths of around 11 km, and 13-15 km. Thus, the Moho depths beneath the island stations may be 13-15 km, which is consistent with the reference crustal model (CRUST1.0) (Fig. S9). Also, the Moho depths agree with other studies (Kim et al., 1998, 2003; Chang and Baag, 2007; Han et al., 2024). The observed Moho depths generally align with the inland rift-flank extension to the rift center, supporting the connection between paleo-rifting and the inland-offshore tectonic transition.

References

Chang, S.-J., and C.-E. Baag (2007), Moho depth and crustal Vp/Vs variation in southern Korea from teleseismic receiver functions: Implication for tectonic affinity between the Korean Peninsula and China, Bulletin of the Seismological Society of America, 97(5), 1621-1631.

Gong, W., Hu, H., Ruan, A., Niu, X., Wang, W., and Tang, Y. (2024), Numerical Modeling on Ocean-Bottom Seismograph P-Wave Receiver Function to Analyze Influences

of Seawater and Sedimentary Layers, Journal of Marine Science and Engineering, 12(11), 2053, doi:10.3390/jmse12112053.

Herrmann, R. B. (2013), Computer programs in seismology: An evolving tool for instruction and research, Seismological Research Letters, 84 (6), 1081-1088, doi:10.1785/0220110096.

Han, J., Han, J., Heo, D., Kim, S., Lee, S., Koh, M. H., Kim, J., Kim, K. B., Ahn, B. S., Jeon, Y., Jo, K., Lim, Y., Lee, S.-J., Kan, T.,-S., Rie, J., and Ahn, U. (2024), Data and early results from temporary seismic arrays for monitoring and investigating magmatic processes beneath Mt. Halla and Ulleung Island volcanoes, South Korea, Geosciences Journal, 28(5), 761-780, doi:10.1007/s12303-024-0027-z.

Hung, T. D., Yang, T., Le, B. M., and Yu, Y. (2019), Effects of failure of the ocean-bottom seismograph leveling system on receiver function analysis, Seismological Research Letters, 90 (3), 1191-1199, doi:10.1785/0220180276.

Kikuchi, M., and Kanamori, H. (1982), Inversion of complex body waves, Bulletin of the Seismological Society of America, 72 (2), 491-506.

Kim, H.-J., Han, S.-J., Lee, G. H., and Huh, S. (1998), Seismic study of the Ulleung Basin crust and its implications for the opening of the East Sea (Japan Sea), Marine Geophysical Researches, 20, 219-237, doi:10.1023/A:1004573816915.

Kim, H.-J., Jou, H.-T., Cho, H.-M., Bijwaard, H., Sato, T., Hong, J.-K., Yoo, H.-S., and Baag, C.-E. (2003), Crustal structure of the continental margin of Korea in the East Sea (Japan Sea) from deep seismic sounding data: evidence for rifting affected by the hotter than normal mantle, Tectonophysics, 364 (1-2), 25-42, doi:10.1016/S0040-1951(03)00048-9.

Laske, G., Masters, G., Ma, Z., and Pasyanos, M. (2013), Update on CRUST1.0 A 1-degree global model of Earth's crust, EGU General Assembly (held 7-12 April, 2013 in Vienna, Austria, EGU2013-2658).

Lee, G. H., Kim, H. J., Suh, M. C., and Hong, J. K. (1999), Crustal structure, volcanism, and opening mode of the Ulleung Basin, East Sea (Sea of Japan), Tectonophysics, 308 (4), 503-525, doi:10.1016/S0040-1951(99)00113-4.

Lee, S. -J., Rhie, J., Kim, S., Kang, T. -S., and Kim, G. B. (2015), Ambient seismic noise tomography of the southern East Sea (Japan Sea) and the Korea Strait, Geosciences Journal, 19, 709-720, doi:10.1007/s12303-015-0012-7.

Ligorría, J. P., and C. J. Ammon (1999), Iterative deconvolution of teleseismic seismograms and receiver function estimation, Bulletin of the Seismological Society of America, 89 (5), 1395-1400.

Park, S., and Hong, T.-K. (2024), Correct off-site determination of seismic sensor orientation from combined analyses of earthquake and microseism records, Bulletin of the Seismological Society of America, 114 (2), 942-954, doi:10.1785/0120230150.

Park, S., and Hong, T.-K. (2024), Continent-side uplifted mantle and geological imprints along a paleo rift in the western East Sea (Sea of Japan), Journal of Geophysical Research: Solid Earth, 129, e2024JB029049, doi:10.1029/2024JB029049.

Wang, Y., and Pavlis, G. L. (2016), Generalized iterative deconvolution for receiver function estimation, Geophysical Journal International, 204 (2), 1086-1099.

Wang, P., Huang, Z., and Wang, X. (2020), A method for estimating the crustal azimuthal anisotropy and Moho orientation simultaneously using receiver functions, Journal of Geophysical Research: Solid Earth, 125 (2), e2019JB018405, doi:10.1029/2019JB018405.

Yang, T., Xu, Y., Du, N., Xu, T., Cao, D., Nan, F., Chu, W., Liang, D., and Hao, T. (2023), Gravity inversion constrained by OBS receiver function reveals crustal structure in Ryukyu Trench, Frontiers in Earth Science, 11, 1187683, doi:10.3389/feart.2023.1187683

Zhu, L., and H. Kanamori (2000), Moho depth variation in southern California from teleseismic receiver functions, Journal of Geophysical Research: Solid Earth, 105(B2), 2969-2980.

Table S1. Local earthquakes used for surface-wave dispersion analysis. The event origin times, locations, focal depths, and magnitudes (M_L) are presented.

No	date (yyyy/mm/dd)	time (hh:mm:ss)	lat (°N)	lon (°E)	dep (km)	M_L
1	2014/03/31	19:48:35	36.95	124.50	8	5.1
2	2016/09/12	10:44:32	35.77	129.19	15	5.1
3	2016/09/12	11:32:54	35.76	129.19	15	5.8
4	2016/09/19	11:33:58	35.74	129.18	14	4.5
5	2017/11/15	05:29:31	36.11	129.37	7	5.4
6	2017/11/15	07:49:30	36.12	129.36	10	4.3
7	2018/02/10	20:03:03	36.08	129.33	14	4.6
8	2019/02/10	03:53:38	36.16	129.90	21	4.1
9	2019/04/19	02:16:43	37.88	129.54	32	4.3
10	2021/08/21	00:40:40	35.70	124.70	7	4.0
11	2021/12/14	08:19:14	33.09	126.16	17	4.9
12	2022/10/29	23:27:49	36.88	127.88	12	4.1
13	2023/05/14	21:27:37	37.87	129.52	28	4.5

Table S2. Teleseismic earthquakes used for receiver function analysis. The event origin times, locations, focal depths, and magnitudes (M_W) are presented.

No	date (yyyy/mm/dd)	time (hh:mm:ss)	lat (°N)	lon (°E)	dep (km)	M_W
1	2019/01/22	5:10:09	-10.37	119.07	19	6.4
2	2019/04/02	21:35:38	52.17	177.97	12	6.4
3	2019/04/06	21:55:04	-6.92	124.86	547	6.3
4	2019/04/12	11:40:57	-1.85	122.56	12	6.8
5	2019/04/29	14:19:54	10.94	57.14	16	6.3
6	2019/05/06	21:19:45	-7.06	146.49	128	7.1
7	2019/05/14	12:58:39	-4.03	152.52	22	7.6
8	2019/06/15	22:55:13	-30.93	-177.79	48	7.3
9	2019/06/19	17:24:57	-2.17	138.53	13	6.3
10	2019/06/24	2:53:44	-6.51	129.17	220	7.3
11	2019/07/06	3:20:05	35.78	-117.58	12	7.0
12	2019/07/07	15:08:47	0.55	126.10	31	6.9
13	2019/07/14	5:39:32	-18.15	120.29	22	6.7
14	2019/07/14	9:11:05	-0.72	128.13	12	7.2
15	2019/07/31	15:02:37	-16.28	167.85	188	6.6
16	2019/08/02	12:03:35	-7.40	104.85	52	6.9
17	2019/09/01	15:54:26	-20.40	-178.51	614	6.7
18	2019/11/04	22:43:41	-18.38	-175.35	12	6.6
19	2019/11/08	10:44:50	-21.94	-179.42	599	6.5
20	2019/11/14	16:17:48	1.66	126.32	30	7.1
21	2019/11/24	0:54:06	51.42	-175.57	24	6.4
22	2020/01/24	17:55:25	38.29	39.02	12	6.8
23	2020/05/02	12:51:10	34.05	25.64	12	6.6
24	2020/05/06	13:54:00	-6.82	129.88	113	6.8
25	2020/05/12	22:41:18	-12.14	166.42	126	6.6
26	2020/06/18	12:50:09	-33.39	-177.55	37	7.4
27	2020/06/25	21:05:24	35.71	82.35	13	6.3
28	2020/07/06	22:54:49	-5.69	110.55	535	6.7

Table S2. (*continued*)

No	date (yyyy/mm/dd)	time (hh:mm:ss)	lat (°N)	lon (°E)	dep (km)	M_W
29	2020/07/17	2:50:28	-7.84	147.74	72	7.1
30	2020/07/22	6:13:16	54.83	-159.28	36	7.8
31	2020/07/22	20:07:25	33.10	86.87	17	6.4
32	2020/08/18	22:24:07	-4.56	100.99	23	6.7
33	2020/08/18	22:29:31	-4.47	100.86	25	7.0
34	2020/08/21	4:09:57	-6.64	123.52	637	6.9
35	2020/10/19	20:55:01	54.48	-159.70	37	7.6
36	2020/10/30	11:51:35	37.78	26.63	12	7.0
37	2021/01/21	12:23:10	5.04	127.30	102	7.0
38	2021/02/07	5:46:01	-3.40	146.09	12	6.3
39	2021/03/04	17:41:39	-29.58	-177.01	43	7.4
40	2021/03/04	19:29:02	-29.11	-176.73	34	8.1
41	2021/04/24	0:23:43	-18.91	-176.12	316	6.5
42	2021/05/14	6:33:15	0.09	96.62	14	6.7
43	2021/06/20	17:05:56	-30.29	-177.52	43	6.5
44	2021/07/29	6:16:20	55.40	-157.32	30	8.2
45	2021/08/14	11:57:50	55.17	-157.45	25	7.0
46	2021/08/18	10:10:11	-14.91	166.83	100	6.9
47	2021/10/02	6:29:25	-21.14	174.66	545	7.3
48	2021/10/09	10:58:36	-21.31	174.38	532	6.9
49	2021/10/11	9:10:30	56.45	-156.63	67	6.9
50	2021/10/12	9:24:09	34.98	26.44	6	6.4
51	2021/12/14	3:20:35	-7.46	121.97	14	7.3
52	2021/12/29	18:26:00	-7.69	127.56	166	7.3
53	2022/01/11	1:07:57	34.86	31.79	26	6.6
54	2022/01/11	11:35:55	52.30	-167.83	17	6.8
55	2022/01/14	9:05:48	-7.10	105.21	40	6.6
56	2022/02/16	20:21:15	-23.84	-179.97	547	6.9

Table S2. (*continued*)

No	date (yyyy/mm/dd)	time (hh:mm:ss)	lat (°N)	lon (°E)	dep (km)	M_W
57	2022/03/31	5:44:15	-22.49	170.44	23	6.9
58	2022/05/09	22:33:12	-3.35	146.42	12	6.3
59	2022/05/22	7:06:33	-26.43	178.50	602	6.3
60	2022/05/26	15:38:08	-22.81	172.11	29	6.6
61	2022/05/27	2:36:08	-8.35	127.11	57	6.3
62	2022/06/04	13:07:31	-18.03	-174.77	243	6.3
63	2022/06/04	23:38:16	51.99	178.34	104	6.4
64	2022/08/14	13:44:28	-32.75	-178.73	47	6.6
65	2022/08/23	14:31:45	-5.30	102.92	50	6.3
66	2022/08/29	3:29:20	-1.06	98.44	12	6.2
67	2022/09/09	23:31:54	-1.99	138.25	18	6.2
68	2022/09/10	23:47:12	-6.42	146.30	100	7.6
69	2022/09/14	11:04:13	-21.29	170.01	148	7.0
70	2022/10/13	22:20:25	-4.99	153.42	90	6.3
71	2022/11/09	9:38:48	-25.86	178.23	642	6.8
72	2022/11/09	10:14:39	-25.60	178.26	635	6.6
73	2022/11/11	10:48:57	-19.24	-172.01	51	7.3
74	2022/11/12	7:09:19	-20.03	-178.27	600	7.0
75	2022/11/18	13:37:23	-4.98	100.31	12	6.9
76	2022/11/22	2:03:17	-9.85	159.60	21	7.0
77	2022/12/04	19:24:24	-15.24	-172.88	52	6.8
78	2022/12/20	10:34:32	40.62	-124.25	17	6.4
79	2023/01/08	12:32:52	-15.06	166.68	29	7.0
80	2023/01/09	17:47:47	-7.19	130.03	92	7.6
81	2023/01/15	22:30:03	1.88	97.77	48	6.1
82	2023/01/18	6:06:18	2.93	127.07	28	7.0
83	2023/02/06	1:18:11	37.55	37.45	15	7.8
84	2023/02/06	1:28:22	37.21	36.84	26	6.8

Table S2. (*continued*)

No	date (yyyy/mm/dd)	time (hh:mm:ss)	lat (°N)	lon (°E)	dep (km)	M_W
85	2023/02/06	10:24:59	38.08	37.22	12	7.7
86	2023/02/20	17:04:32	36.06	36.03	12	6.3
87	2023/02/23	0:37:43	38.16	73.22	15	6.8
88	2023/02/23	20:02:52	3.39	127.96	110	6.4
89	2023/02/25	21:24:55	-6.34	149.97	46	6.3
90	2023/03/01	5:36:18	-4.82	149.59	597	6.6
91	2023/03/02	18:04:40	-14.95	166.46	12	6.5
92	2023/03/04	6:41:28	-29.60	-178.58	215	6.9
93	2023/03/16	0:56:22	-30.14	-176.22	12	7.0
94	2023/03/21	16:47:25	36.44	70.78	192	6.6
95	2023/04/02	18:04:19	-4.34	143.21	63	7.1
96	2023/04/14	9:55:52	-6.19	112.16	607	7.1
97	2023/04/22	8:23:48	-5.22	125.53	18	6.3
98	2023/04/24	0:42:04	-29.94	-177.39	46	7.1
99	2023/04/24	20:01:11	-0.70	98.57	28	7.0
100	2023/05/10	16:02:11	-15.57	-174.48	205	7.6
101	2023/05/19	2:57:20	-23.35	170.91	20	7.7
102	2023/05/20	1:51:08	-23.04	170.33	17	6.2
103	2023/06/15	18:06:36	-22.98	-176.79	183	7.2
104	2023/07/02	10:27:50	-17.84	-174.75	240	6.9
105	2023/07/16	6:48:30	54.44	-160.90	32	7.2
106	2023/07/26	12:44:42	-14.69	167.98	12	6.4
107	2023/10/07	6:41:06	34.59	61.96	12	6.2
108	2023/10/07	8:40:20	-5.49	146.07	53	6.9
109	2023/10/11	0:41:58	34.59	62.03	12	6.2
110	2023/10/15	3:36:03	34.62	62.09	12	6.3
111	2023/10/16	11:35:35	52.54	-176.86	187	6.4
112	2023/11/01	21:04:51	-10.01	123.68	43	6.1

Table S2. (*continued*)

No	date (yyyy/mm/dd)	time (hh:mm:ss)	lat (°N)	lon (°E)	dep (km)	M_W
113	2023/11/08	4:53:54	-6.32	129.51	13	7.2
114	2023/11/08	13:02:15	-6.14	129.89	13	6.8
115	2023/11/14	7:01:02	-4.05	87.02	12	6.1
116	2023/11/27	21:46:52	-3.32	143.99	12	6.5
117	2023/12/07	12:56:40	-20.53	169.14	44	7.0
118	2024/01/11	9:20:32	36.48	70.36	218	6.4
119	2024/01/22	18:09:15	41.19	78.57	14	7.0

Table S3. Crustal thicknesses and V_P/V_S ratios beneath stations. The station locations, Moho depths (H), V_P/V_S ratios, and numbers of analyzed events (N) are presented.

station	lat (°N)	lon (°E)	N	H (km)	V_P/V_S
AGSA	37.0917	127.8081	65	32.4	1.742
AGSA	37.0917	127.8081	65	32.4	1.742
BKWA	37.1681	127.9875	59	32.5	1.758
BURB	37.2317	127.7486	75	32.8	1.703
BUSA	36.9792	128.6610	39	34.8	1.628
CGIA	37.5822	128.1527	62	33.2	1.668
CGUB	37.5583	127.7136	80	31.4	1.718
CHC2	37.7776	127.8145	64	32.2	1.700
CHJ3	36.8730	127.9748	73	34.8	1.650
CHNB	38.2710	127.1211	90	31.3	1.703
CRB	37.3899	127.9589	51	34.8	1.633
CWO2	38.0834	127.5205	74	30.6	1.789
DDCA	37.9021	127.0610	67	30.7	1.745
DGLA	36.7906	128.2705	66	31.0	1.795
DGY2	37.6904	128.6742	31	31.6	1.813
DKSA	36.9044	128.1455	68	33.2	1.712
DNYA	36.9877	128.3559	50	32.7	1.742
GAGA	37.1307	129.1697	63	31.4	1.703
GAPB	37.8441	127.4950	71	31.0	1.748
GEJB	38.4165	128.3858	67	26.4	1.796
GGSA	36.9296	129.1518	69	31.6	1.719
GLCA	37.9049	128.5207	72	31.7	1.730
GMHB	38.2500	127.4209	74	33.4	1.614
GW01	37.2741	128.0799	27	32.4	1.764
GW02	37.4508	128.3024	25	33.4	1.736
GW03	37.3558	128.5207	24	35.2	1.690
GW04	37.3016	128.9167	30	30.1	1.809
GW05	37.6337	128.8558	27	30.0	1.808
GW06	37.6879	128.5603	29	32.2	1.712

Table S3. (*continued*)

station	lat (°N)	lon (°E)	N	H (km)	V_P/V_S
GW07	37.6322	128.3514	25	32.5	1.738
GW08	37.6682	128.0151	26	32.4	1.738
GW09	37.7907	127.6429	24	30.8	1.759
GW10	37.9814	127.6077	25	30.1	1.791
GW11	37.9241	127.9492	26	31.2	1.715
GW12	38.0186	128.4748	22	31.3	1.734
GW13	38.2209	128.3696	23	30.8	1.767
GW14	37.5790	128.5564	26	34.7	1.660
GW15	38.1883	127.8000	25	31.3	1.706
GW16	38.2671	127.2824	20	30.7	1.729
GW17	37.5886	128.7766	26	32.4	1.755
GW18	37.2872	129.2546	29	26.5	1.832
GW19	37.8488	128.7258	20	29.9	1.767
GW20	37.1175	128.6450	19	33.5	1.691
GWLA	37.2196	128.8213	66	33.7	1.672
HESA	37.5407	127.9564	63	32.3	1.743
HOCA	37.6837	127.8802	65	32.6	1.688
HWCA	38.0650	127.7746	69	32.7	1.638
HWDB	37.6322	127.3404	104	30.0	1.718
ICN2	37.2917	127.4213	71	31.1	1.712
IJA2	37.9865	128.1111	63	33.2	1.601
IJAA	37.9471	128.3247	60	31.6	1.669
IJBA	38.1208	128.3173	45	31.6	1.686
IMWB	37.2380	129.3419	58	26.1	1.732
IYPA	37.4914	127.5218	52	31.0	1.698
JAEA	36.8001	128.9903	66	30.4	1.766
JCUA	37.2753	128.2694	67	34.2	1.685

Table S3. (*continued*)

station	lat (°N)	lon (°E)	N	H (km)	V_P/V_S
JECB	37.1595	128.1945	68	33.1	1.746
JESA	37.4303	128.6654	59	34.5	1.698
JGJA	37.7047	128.9134	47	27.3	1.814
JHCB	38.2322	127.6888	60	31.6	1.705
JJBA	37.6479	128.5645	47	33.2	1.688
JMJ2	37.8816	128.7561	82	27.6	1.837
JOGB	37.6210	128.9801	56	25.5	1.867
JSB	37.3175	128.6854	96	35.0	1.646
KAWA	37.8043	128.8547	66	26.8	1.825
KNUC	37.8727	127.7427	75	32.4	1.668
KNUD	37.2257	129.0976	74	30.8	1.773
KOSB	38.6028	128.3596	58	20.5	1.893
KSA	38.5953	128.3516	88	19.9	1.949
LMGA	37.4910	128.8638	67	31.5	1.758
MGB	36.6402	128.2146	76	32.1	1.753
MOGA	37.6962	127.5825	66	31.8	1.671
NAMB	37.7711	128.3863	92	32.8	1.659
NCNA	37.8197	128.0919	67	32.6	1.675
OJSA	36.7869	128.5714	48	33.4	1.690
PCH	37.9645	127.1320	67	31.6	1.714
PGEA	36.7560	128.6921	63	33.4	1.651
PYCA	37.5620	128.3778	64	33.3	1.706
PYCB	37.3775	128.3947	77	35.6	1.640
SESA	37.7200	128.1735	66	32.2	1.703
SGMA	37.8280	127.2880	66	31.4	1.719
SH2B	38.2686	128.2525	69	30.7	1.738
SKC2	38.2899	128.5219	67	21.5	1.977

Table S3. (*continued*)

station	lat (°N)	lon (°E)	N	H (km)	V_P/V_S
SLSA	37.1349	127.5196	69	31.9	1.721
SND	37.1579	128.7962	94	34.2	1.644
SNDA	37.2617	128.5956	57	35.8	1.651
SNGB	37.3465	129.0862	47	31.1	1.699
SUBA	36.7826	129.2211	59	30.3	1.791
TBA2	37.1225	128.9524	60	33.2	1.643
TOHA	37.5070	129.1238	59	27.2	1.789
UJNA	36.9926	129.4136	64	22.2	1.976
WJU2	37.4034	128.0527	25	33.7	1.705
Y025	38.1093	127.0770	32	30.7	1.716
Y028	37.6558	127.3066	64	30.0	1.724
Y029	37.9387	127.2205	56	31.8	1.696
Y030	38.1050	127.2051	57	29.9	1.801
Y057	37.8133	127.3473	48	30.1	1.802
Y058	38.0567	127.3811	51	31.9	1.707
Y059	37.8049	127.4854	51	30.7	1.752
Y060	37.4916	127.5982	53	30.4	1.743
YAGA	37.4070	127.7568	68	31.2	1.757
YAPA	37.4890	127.4942	19	30.9	1.708
YAYA	38.1438	128.6025	71	23.8	1.970
YAYB	38.0225	128.7160	71	26.5	1.807
YGGA	38.0980	127.9852	70	31.9	1.683
YKB	38.2254	127.9903	89	31.9	1.674
YOGA	38.0942	127.2765	66	30.4	1.802
YOJB	36.8720	128.5166	75	32.7	1.739
YOW2	37.1812	128.4569	69	34.4	1.725
YSUM	37.2826	127.9034	63	33.9	1.680

Table S4. Information of offshore stations including two permanent island stations (ULDR and DOKDO) and two ocean bottom seismometer stations (E208 and E209). The locations (latitudes, longitudes, and elevations) and data collection periods are presented.

No	station	lat (°N)	lon (°E)	elev (m)	data collection period
1	ULDR	37.4809	130.8987	269	Jan 1, 2019 to Jan 31, 2024
2	DOKDO	37.2393	131.8696	166	Jan 1, 2019 to Jan 31, 2024
3	E208	37.3136	129.9252	-1198	Jul 17, 2022 to May 17, 2023
4	E209	37.1691	129.9845	-1481	Jul 17, 2022 to May 15, 2023

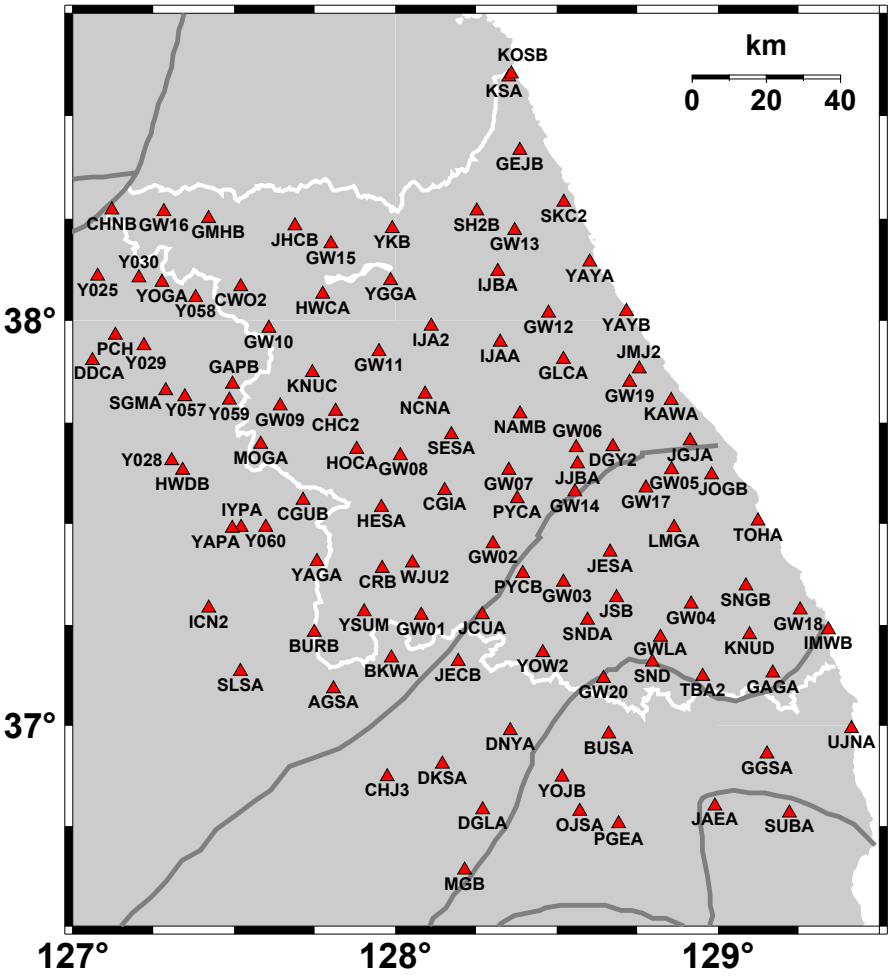

Figure S1. Map of seismic stations used in this study.

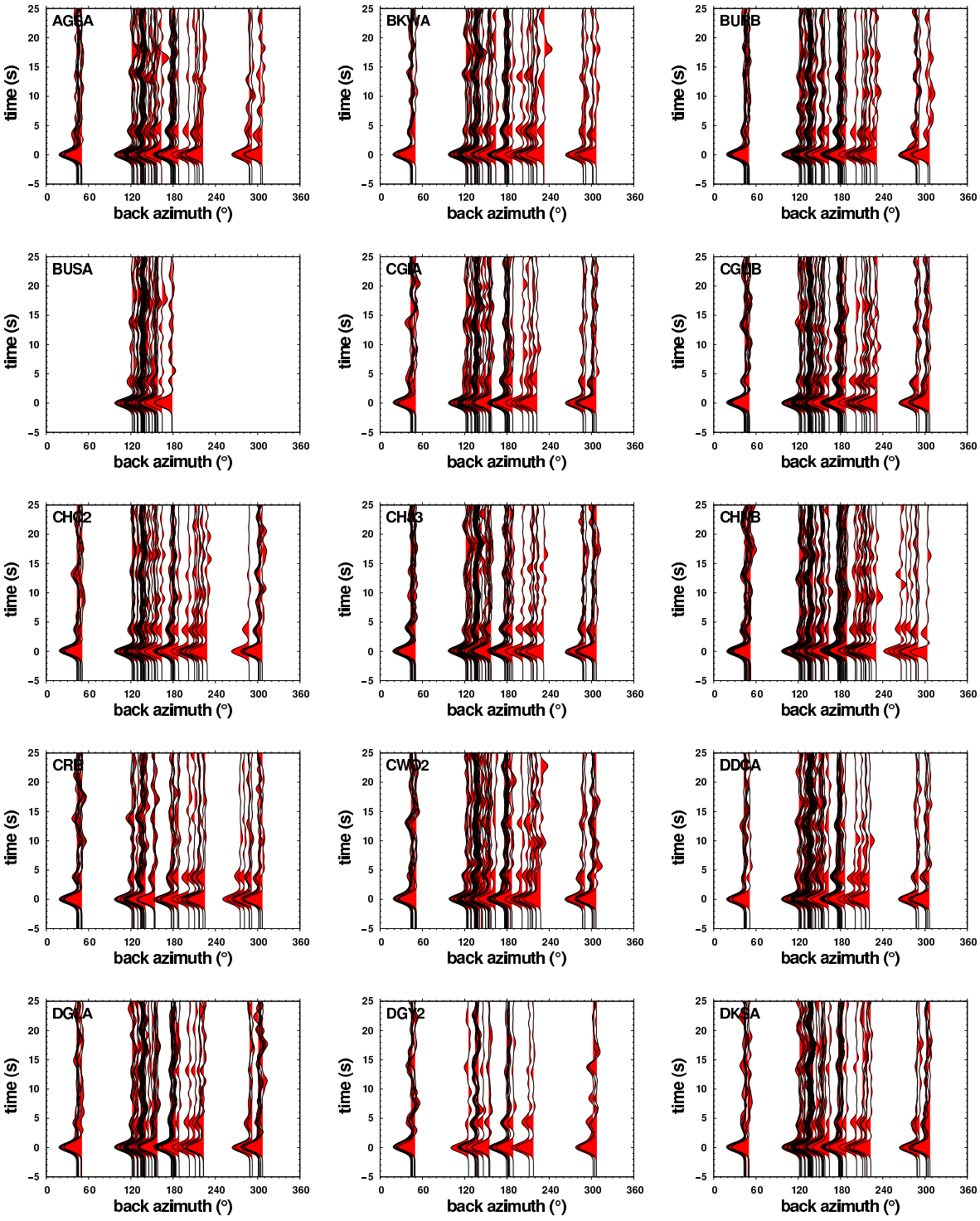

Figure S2. Receiver function profiles with Gaussian filter parameters of $\alpha = 1.0$ as a function of back azimuth for each station.

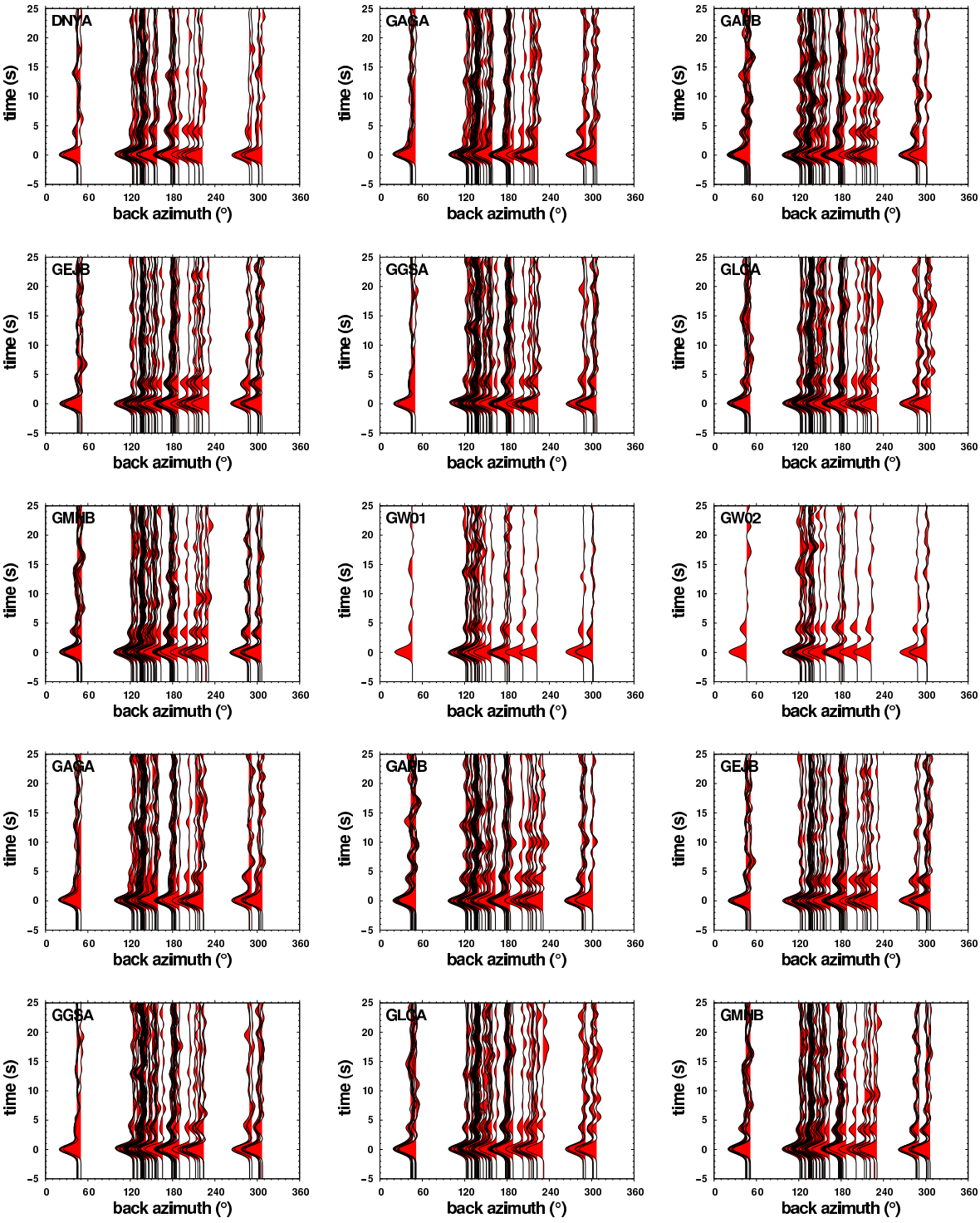

Figure S2. (*continued*)

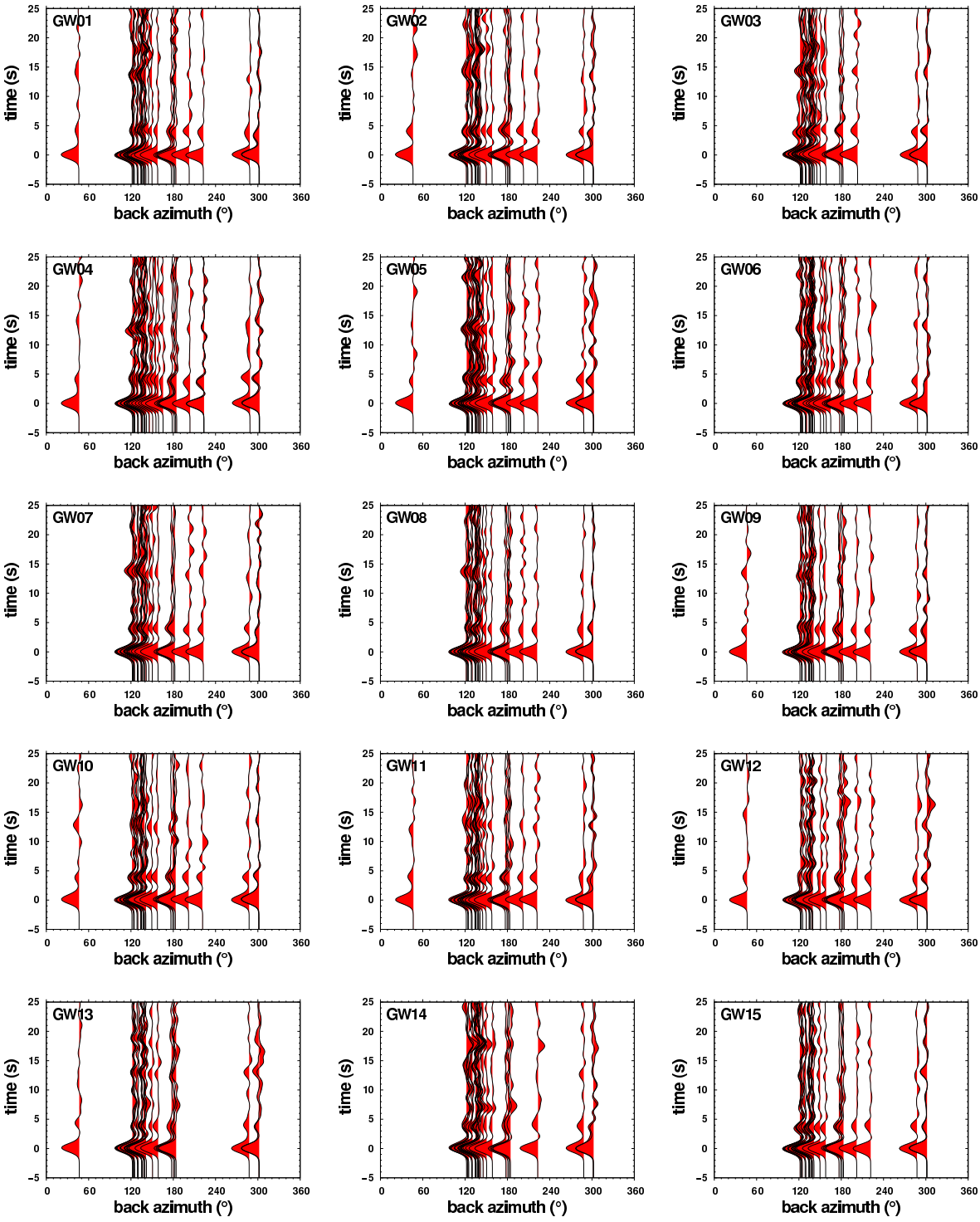

Figure S2. (*continued*)

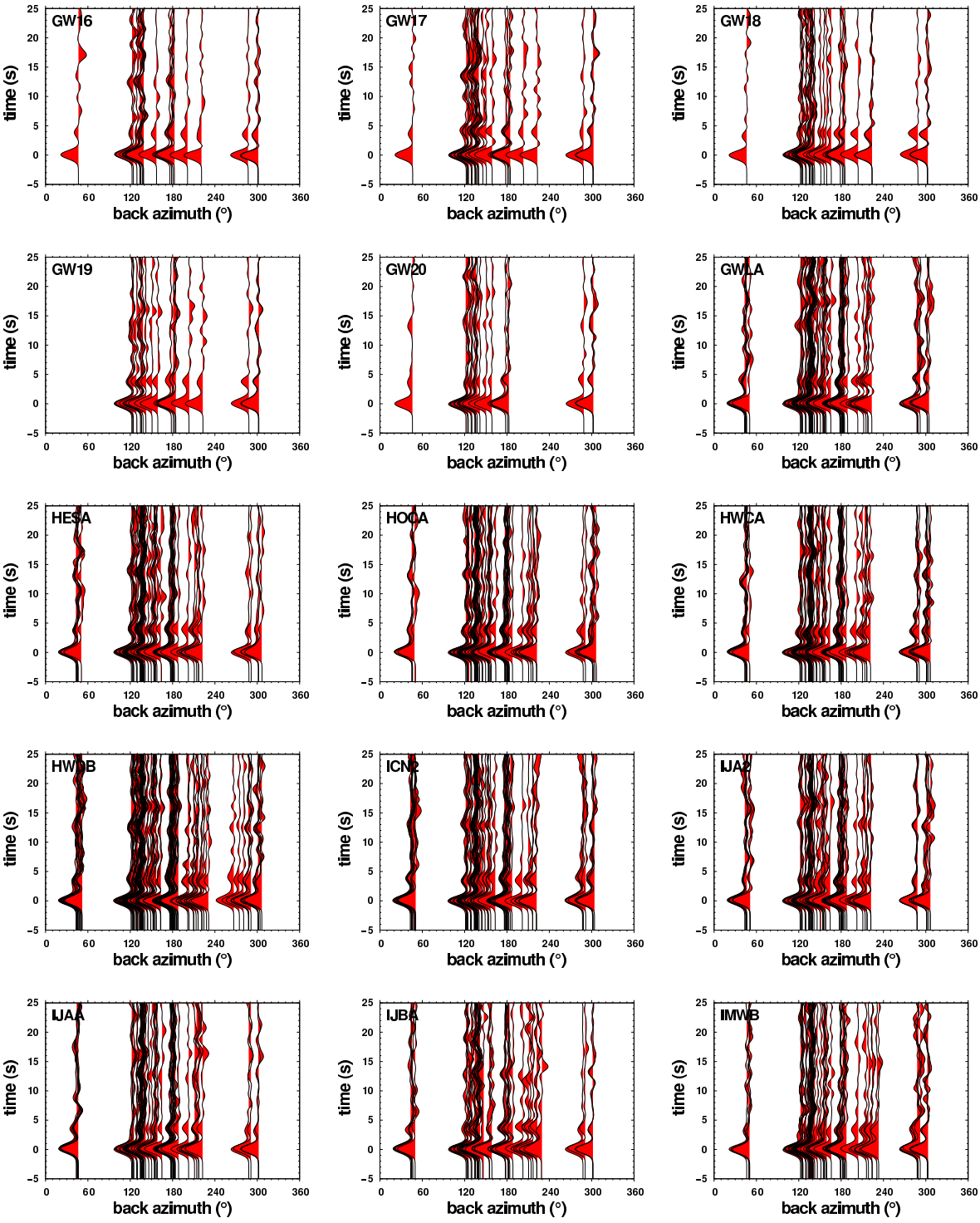

Figure S2. (*continued*)

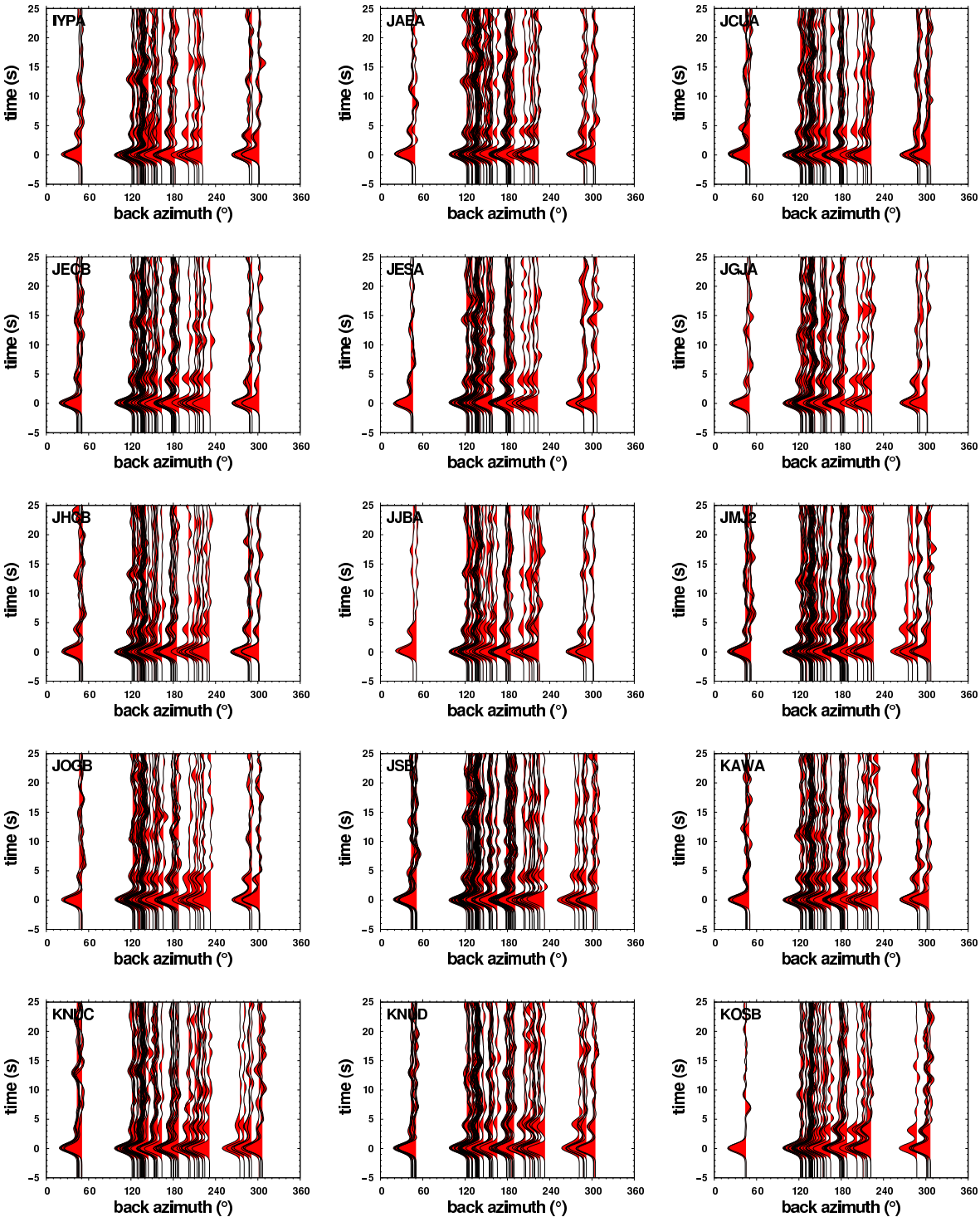

Figure S2. (*continued*)

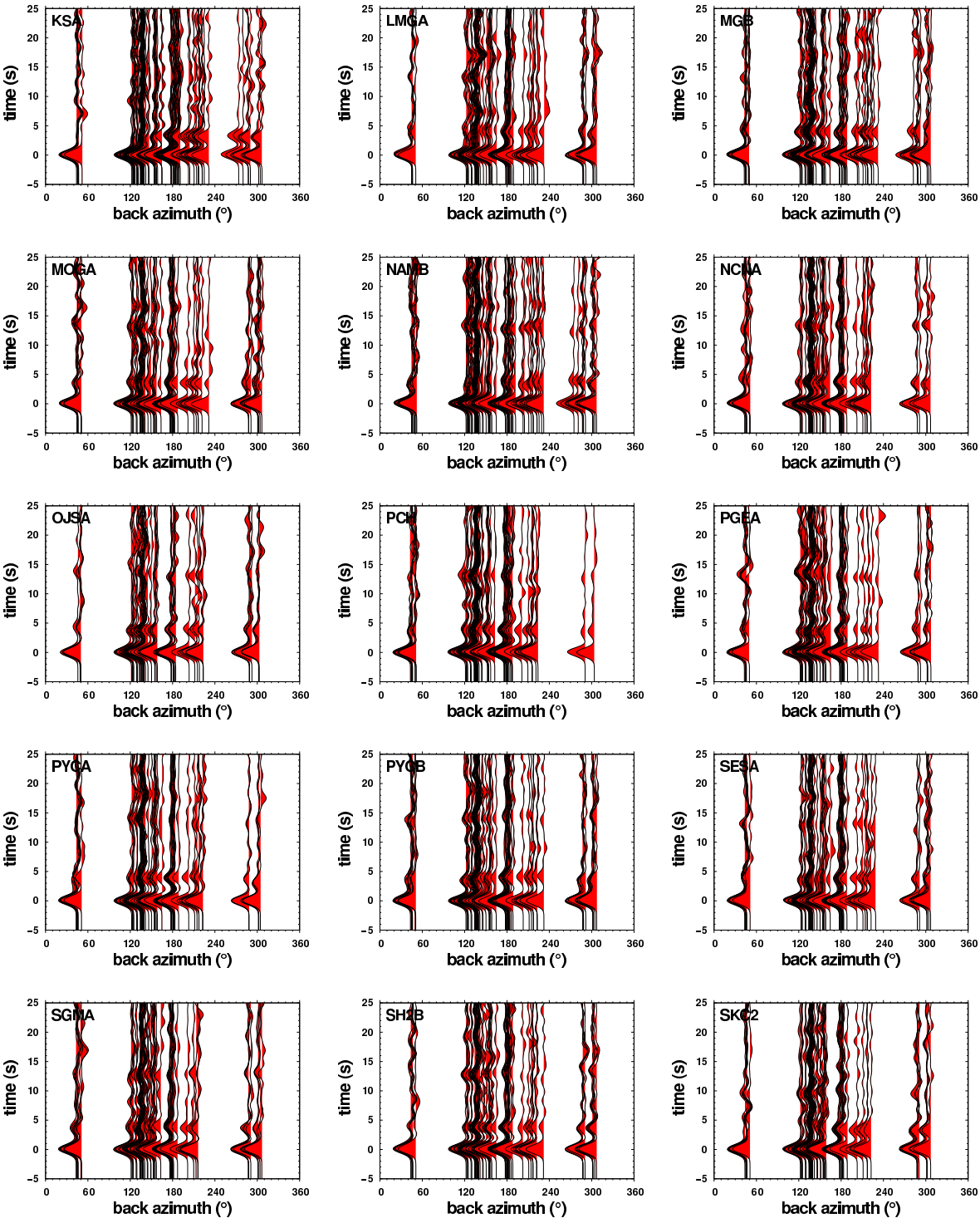

Figure S2. (*continued*)

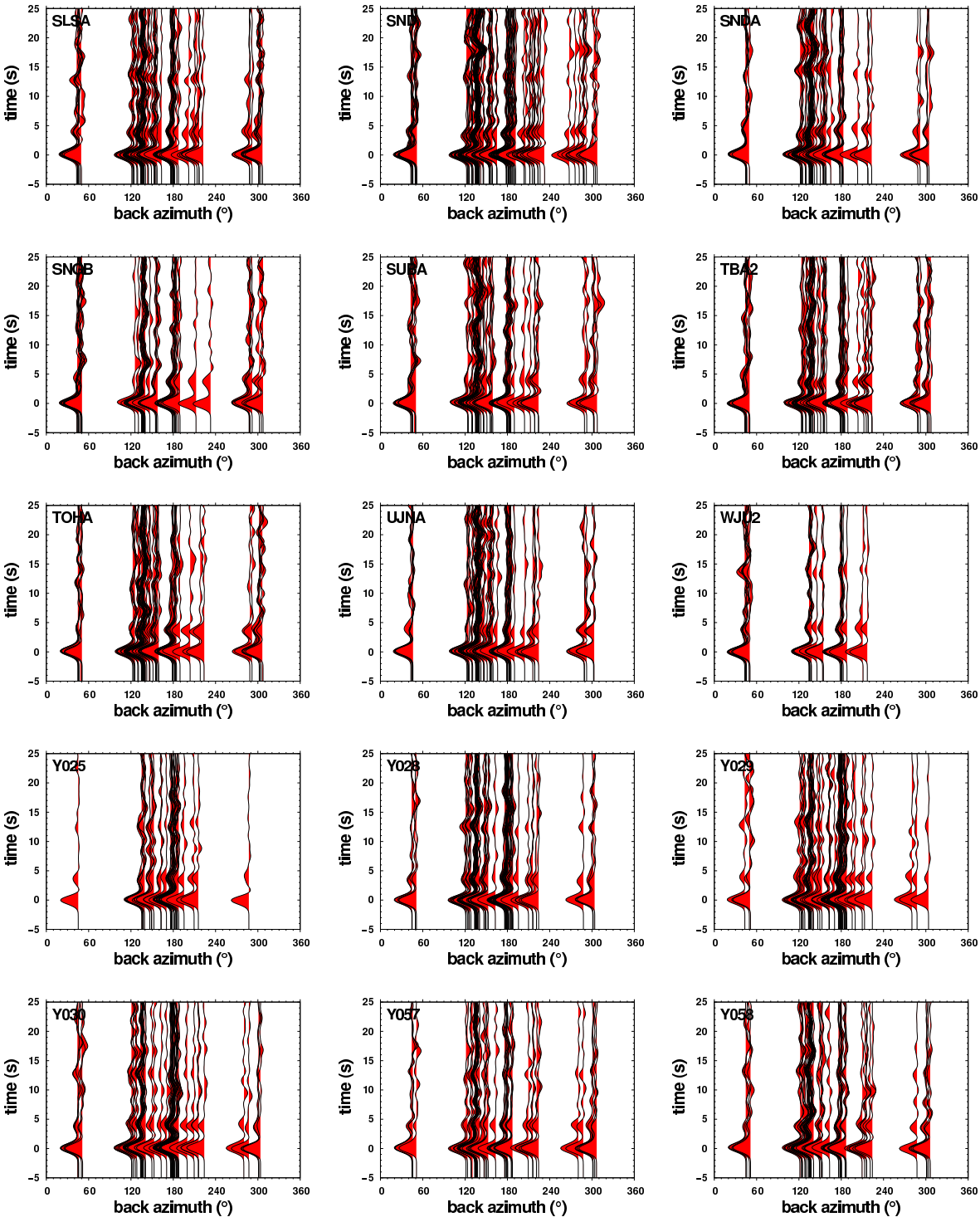

Figure S2. (*continued*)

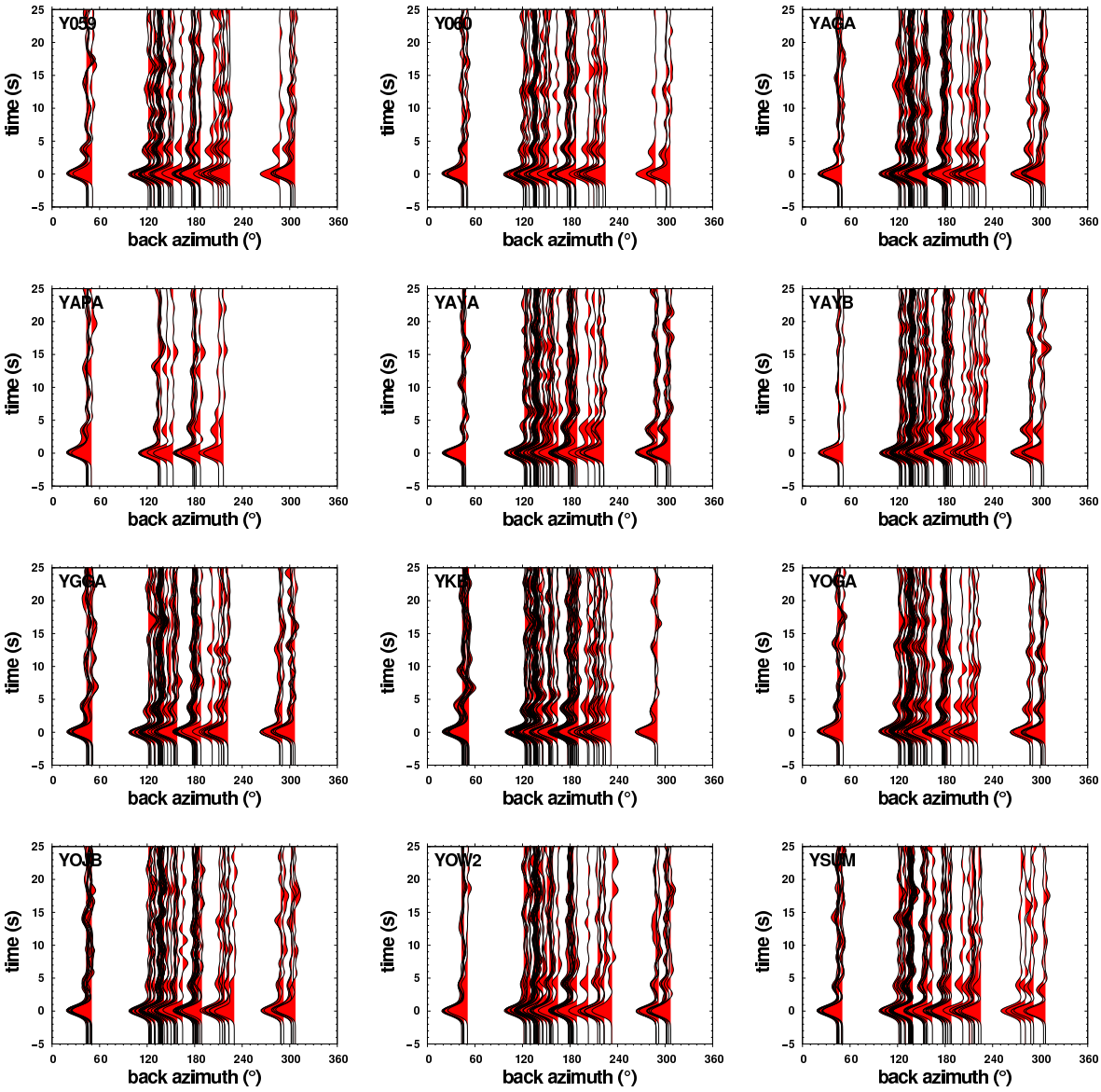

Figure S2. (*continued*)

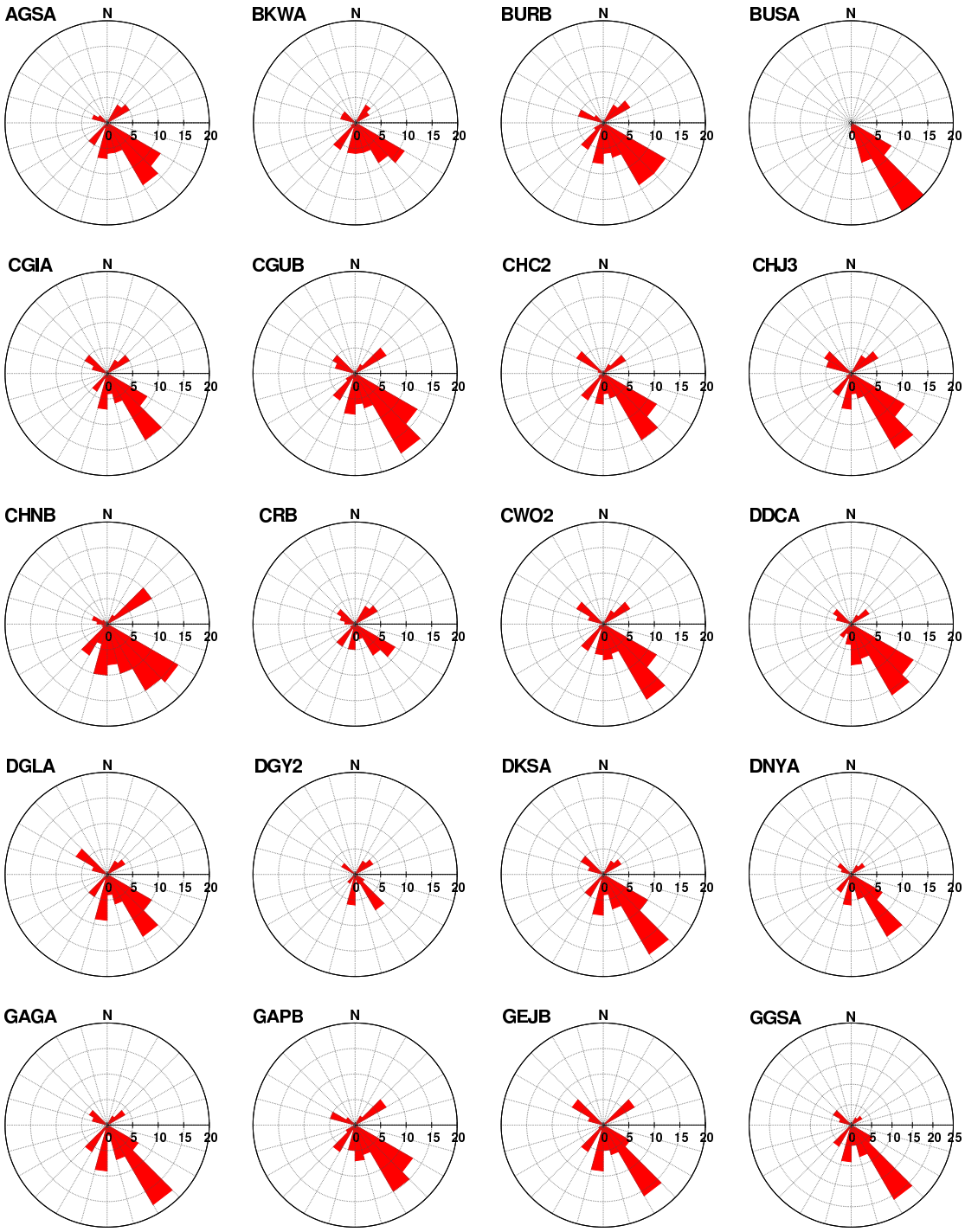

Figure S3. Azimuth distribution of earthquakes used in the receiver function analysis for each station.

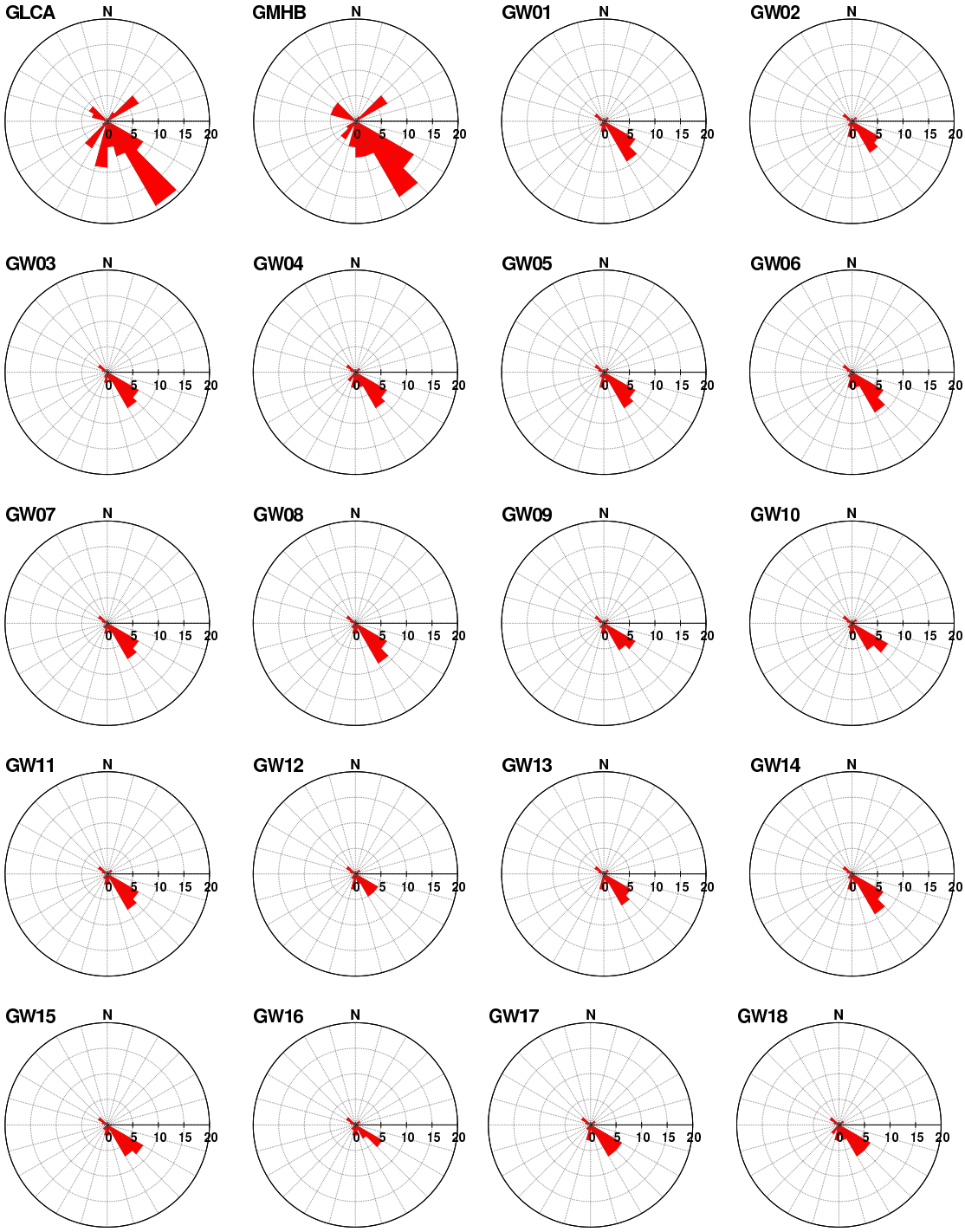

Figure S3. (*continued*)

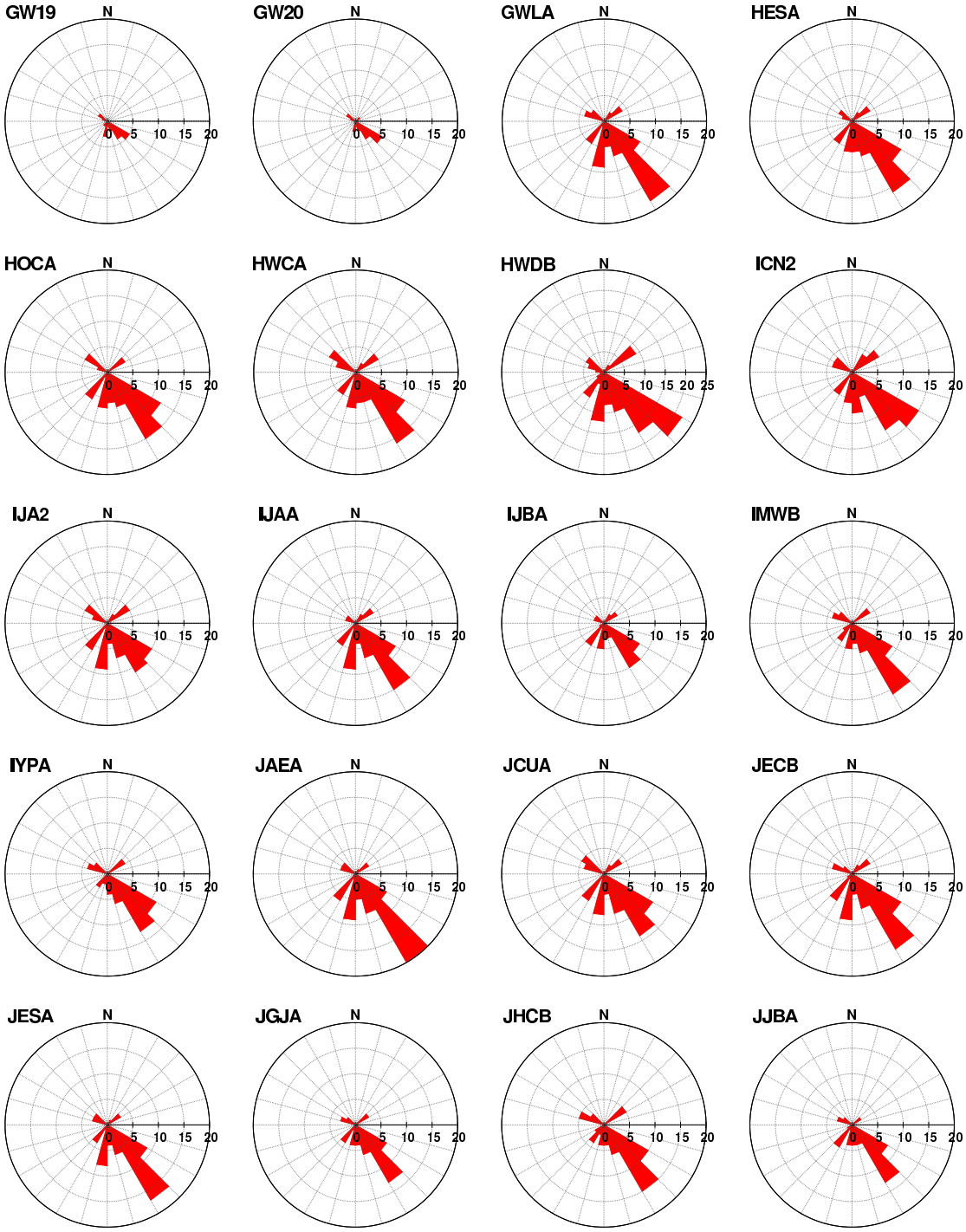

Figure S3. (*continued*)

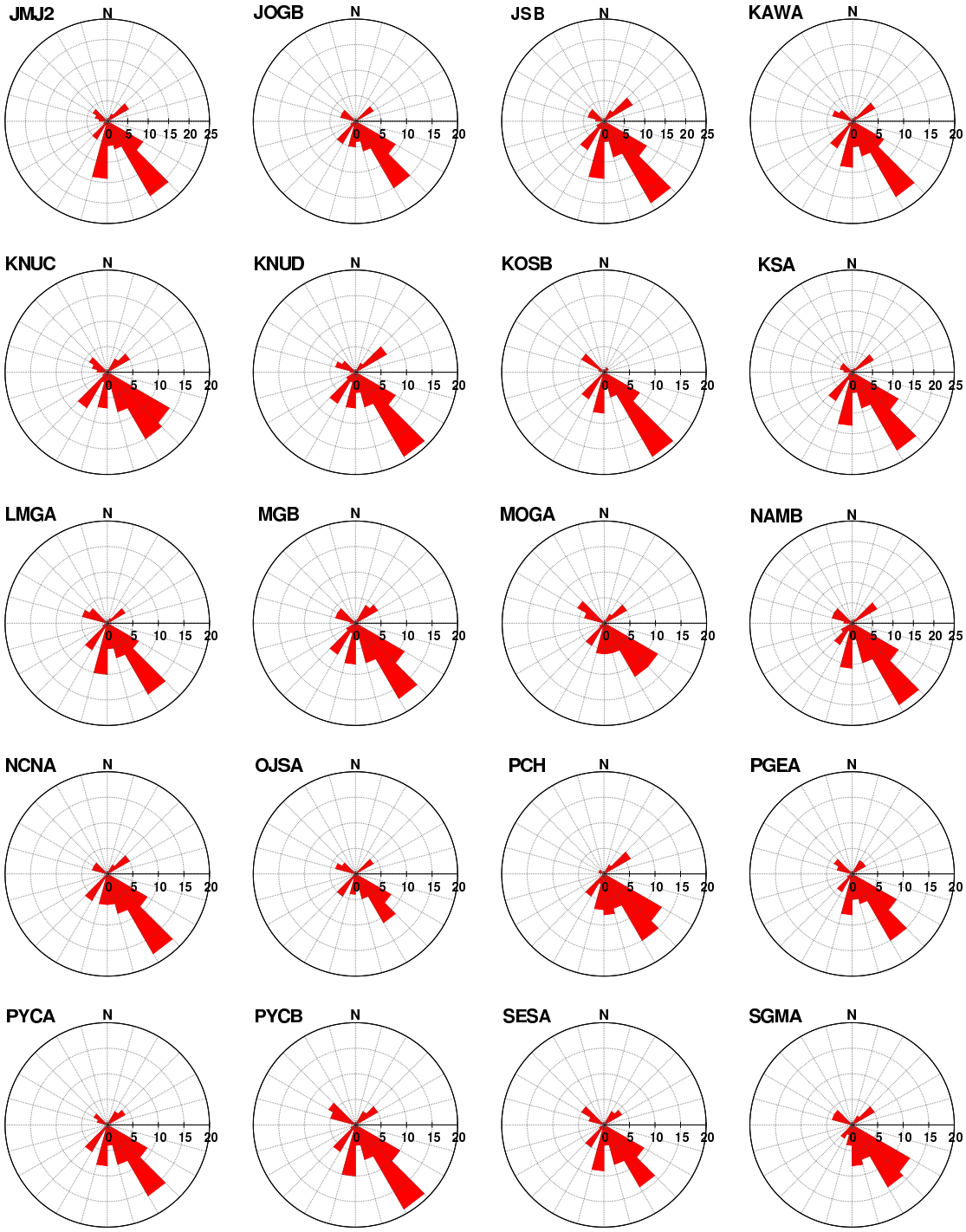

Figure S3. (*continued*)

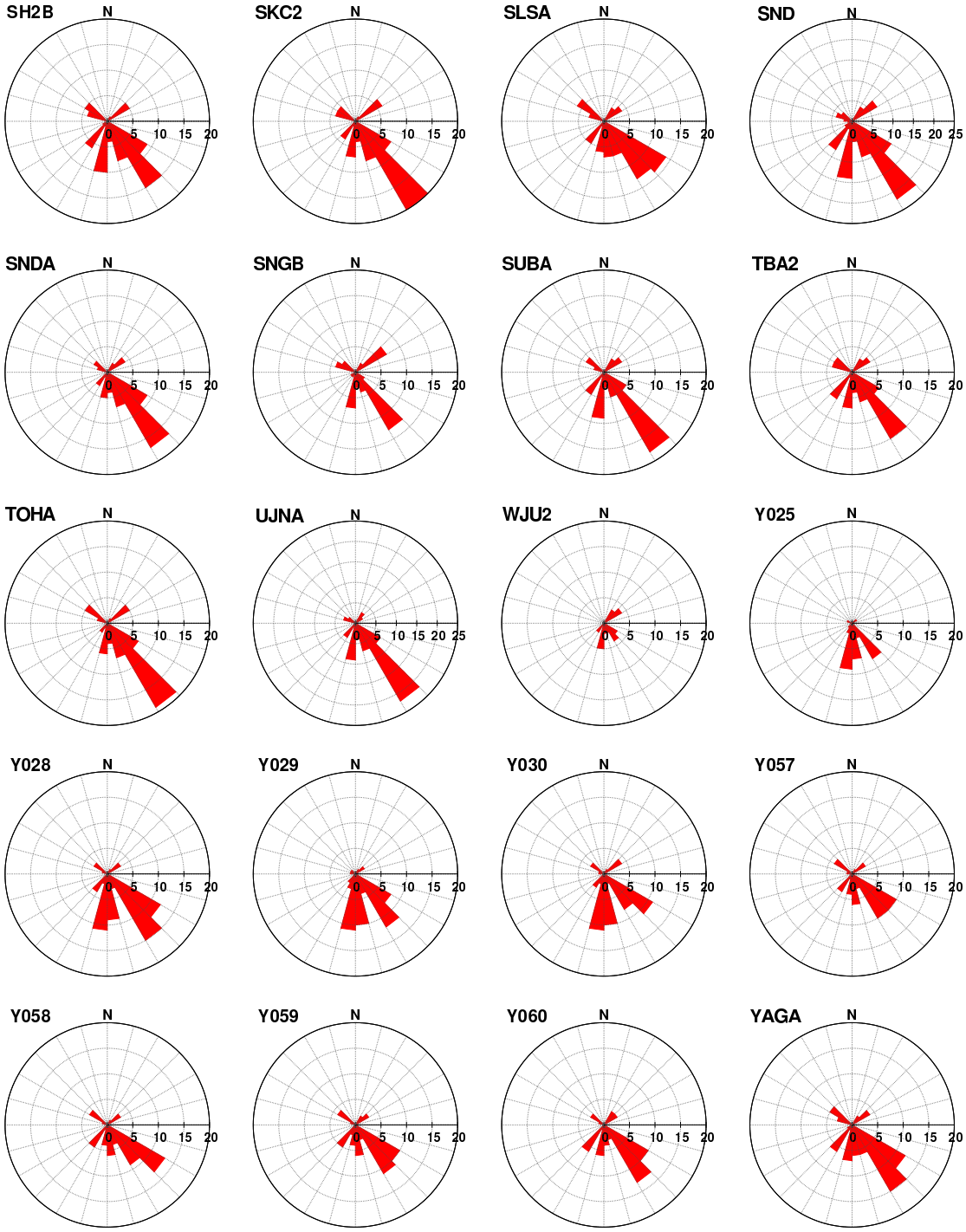

Figure S3. (*continued*)

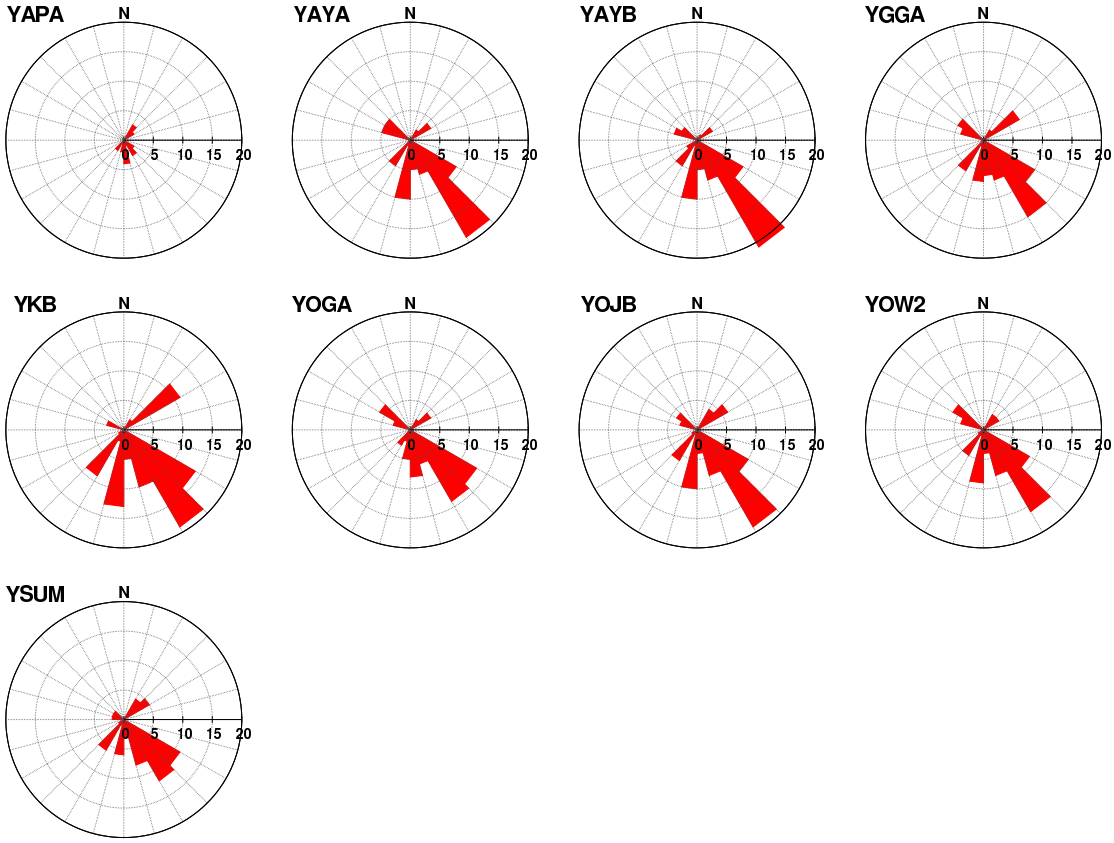

Figure S3. (*continued*)

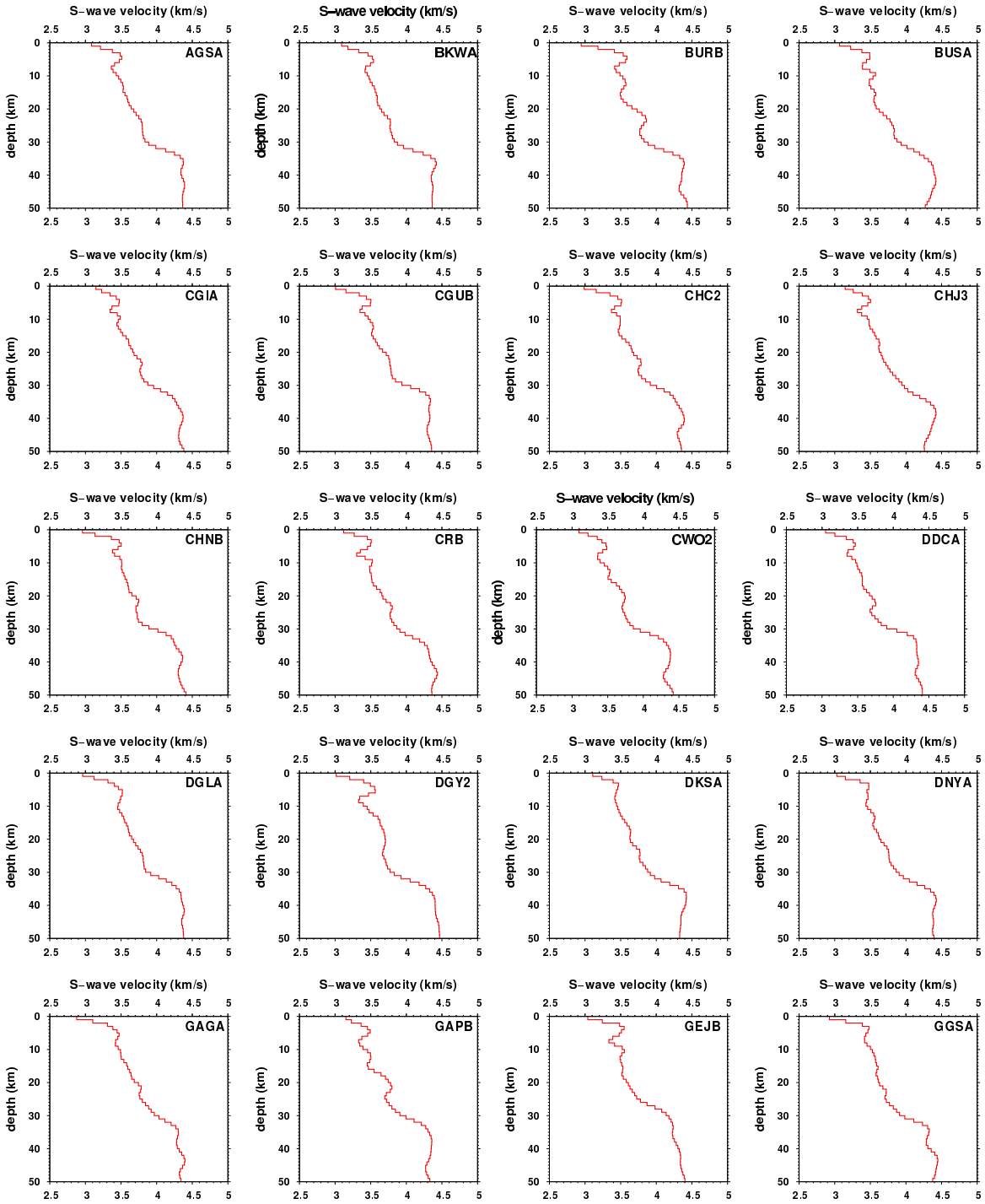

Figure S4. Inverted shear-wave velocity models by joint inversion with influence factors of $\gamma = 0.15$ and damping factor of $\eta = 0.5$ at each station.

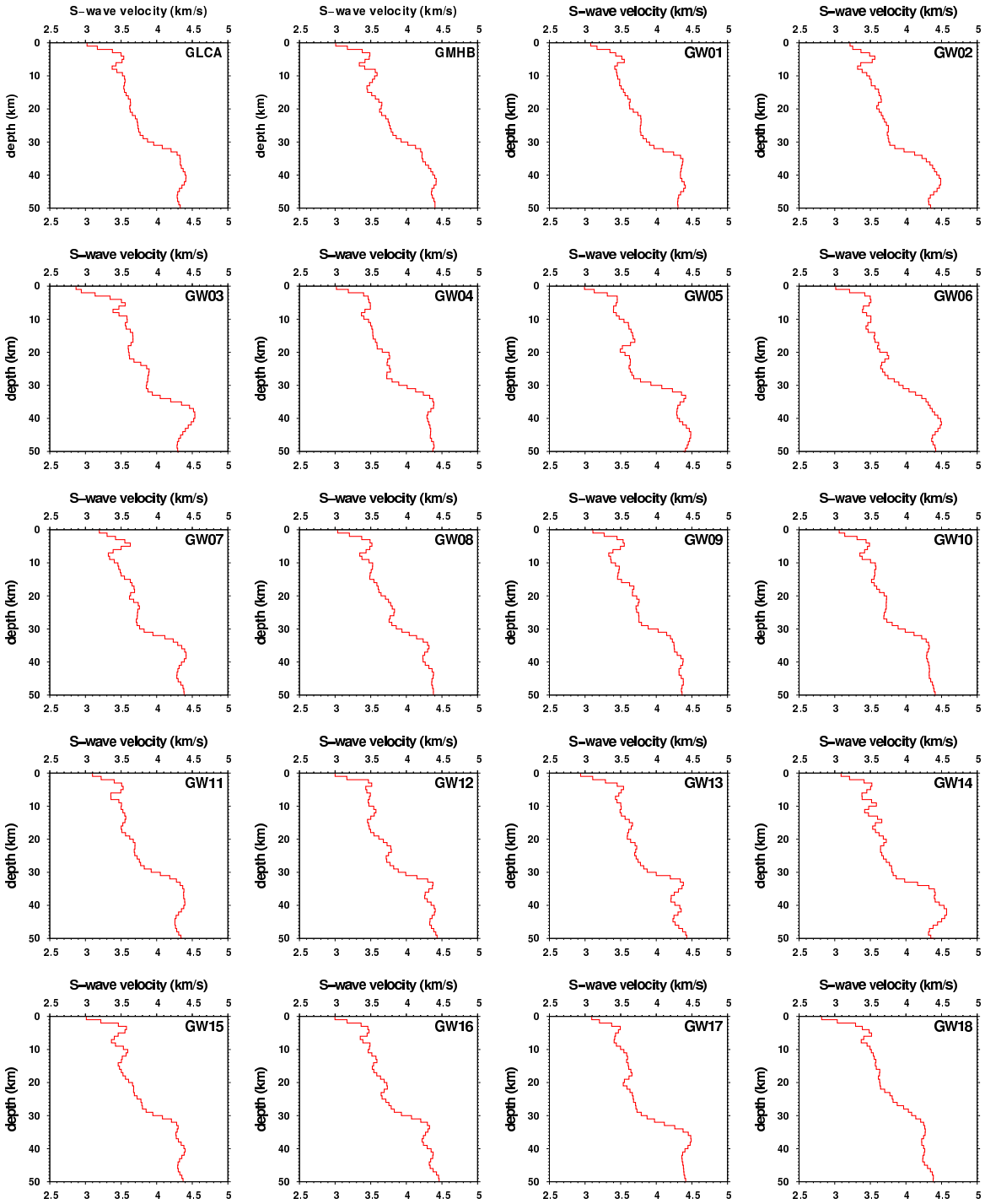

Figure S4. (*continued*)

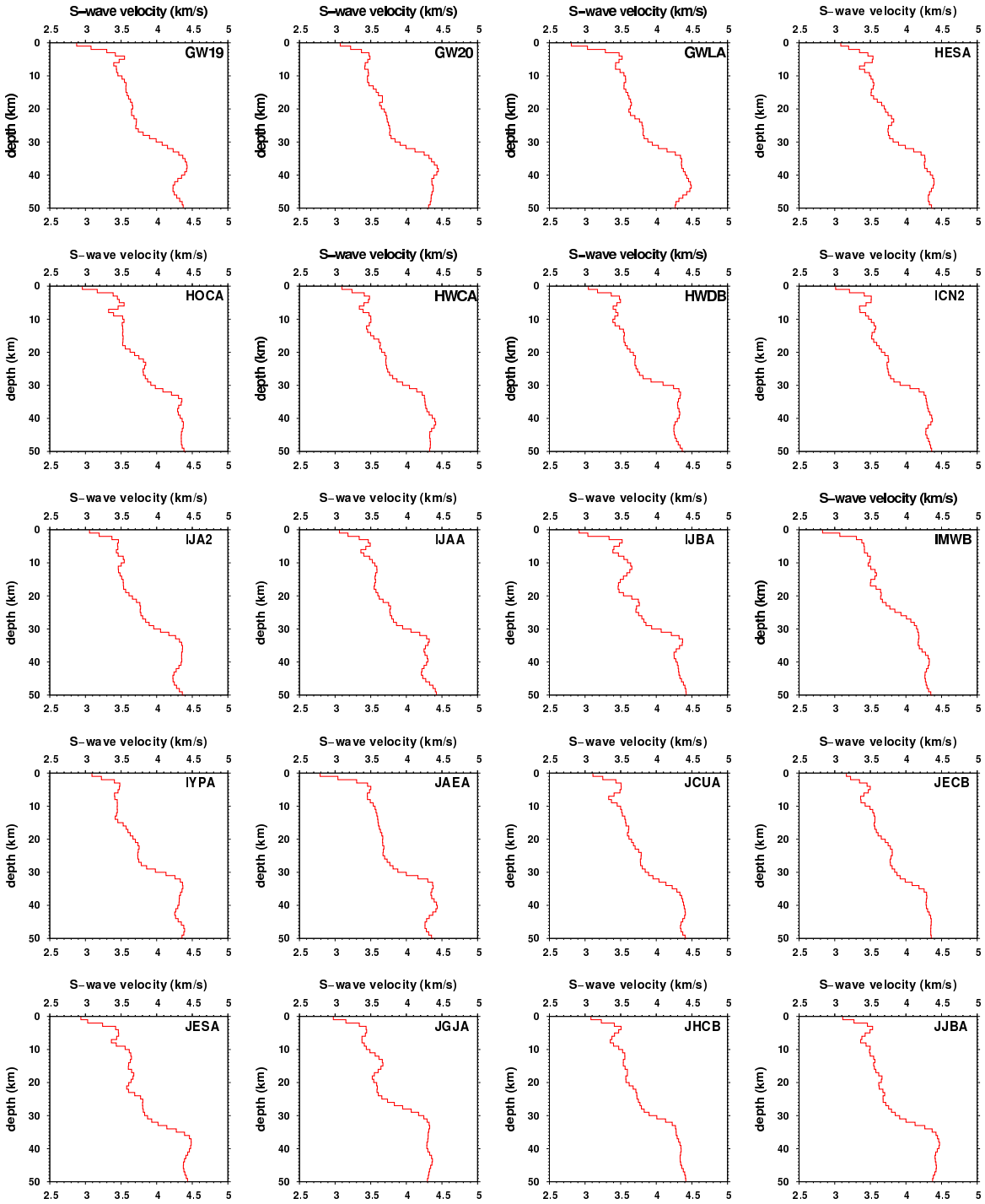

Figure S4. (*continued*)

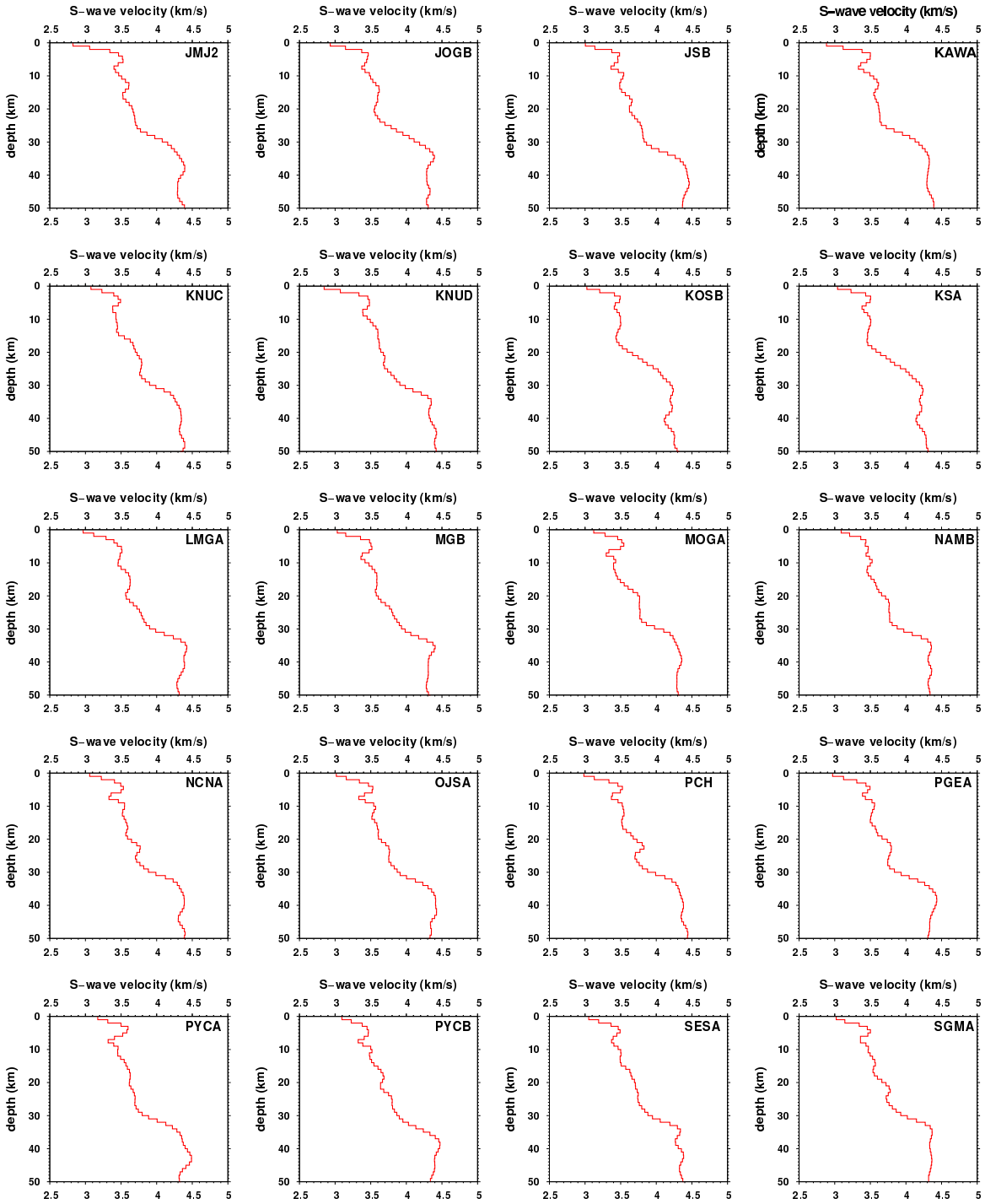

Figure S4. (*continued*)

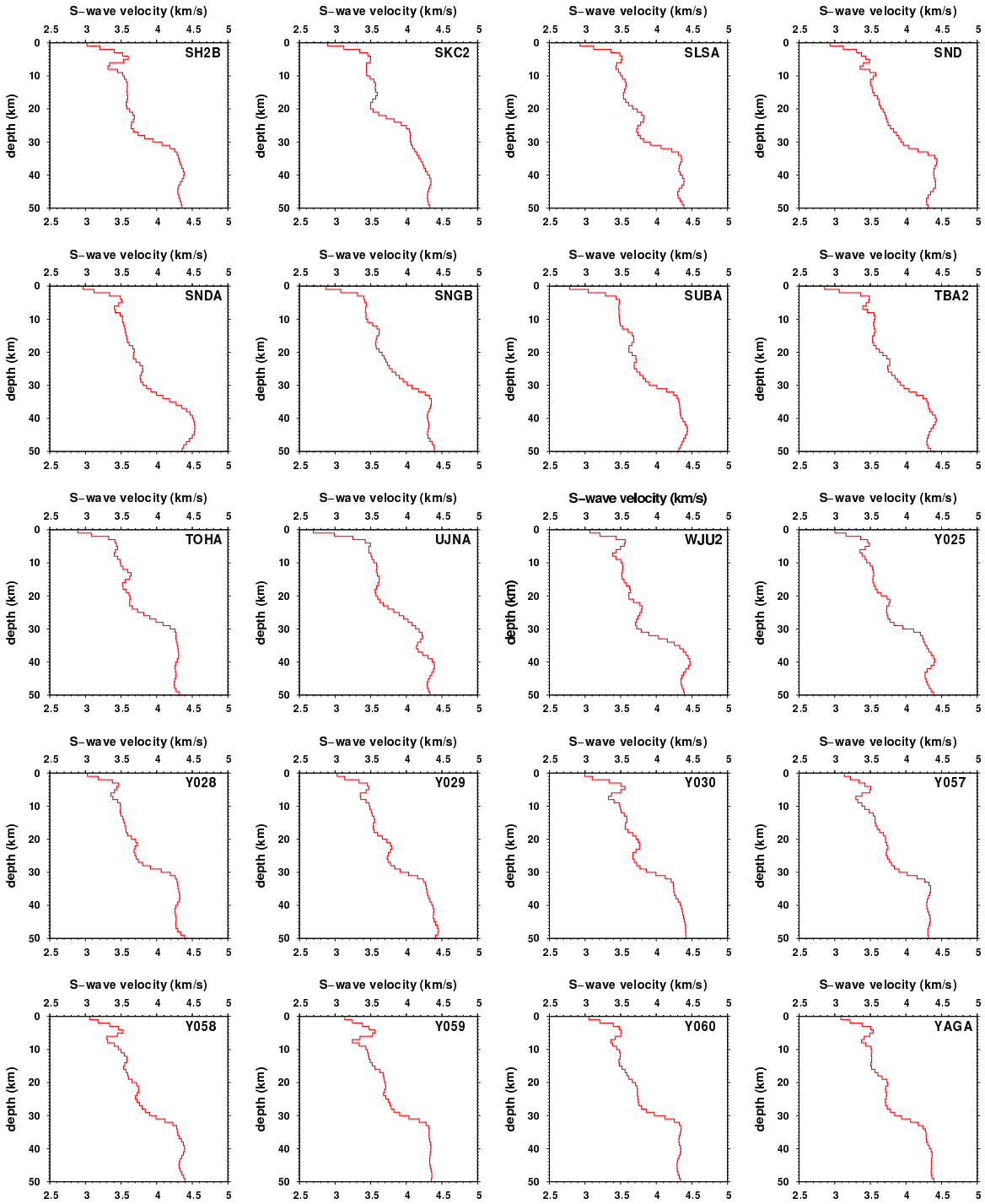

Figure S4. (*continued*)

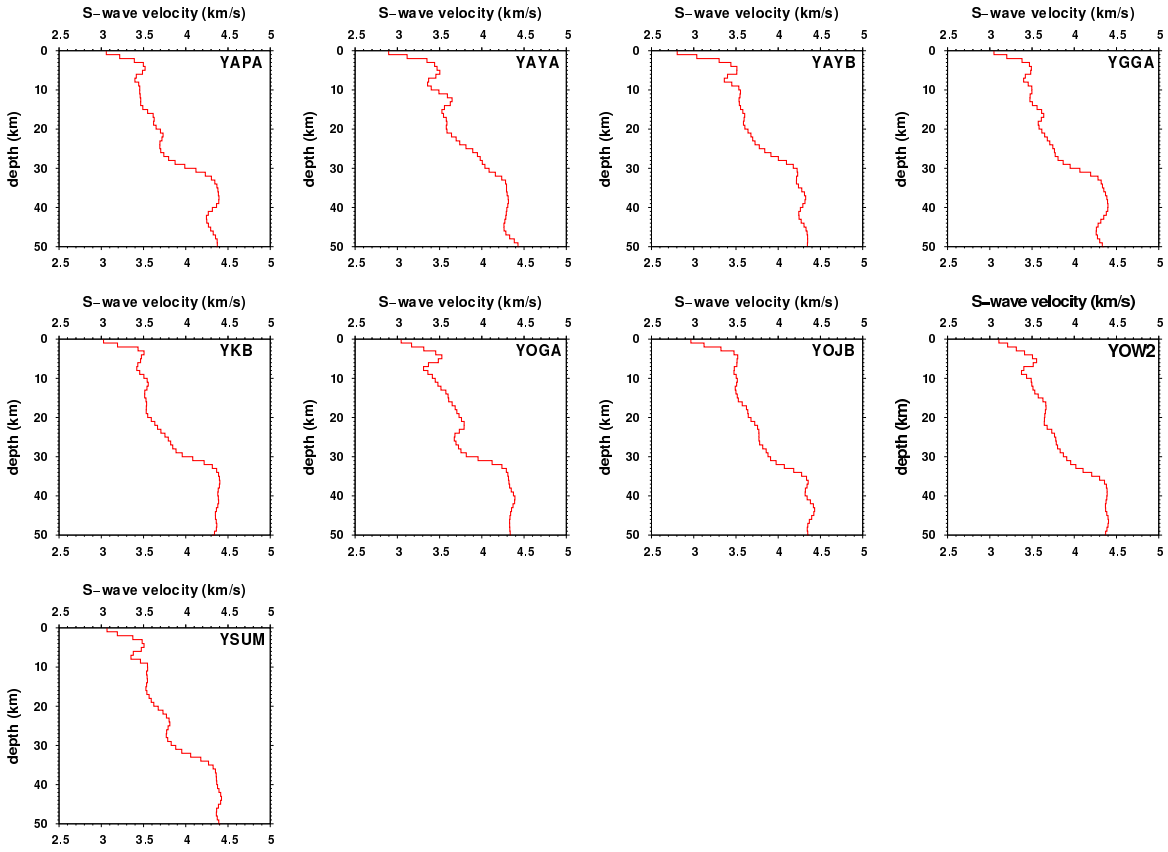

Figure S4. (*continued*)

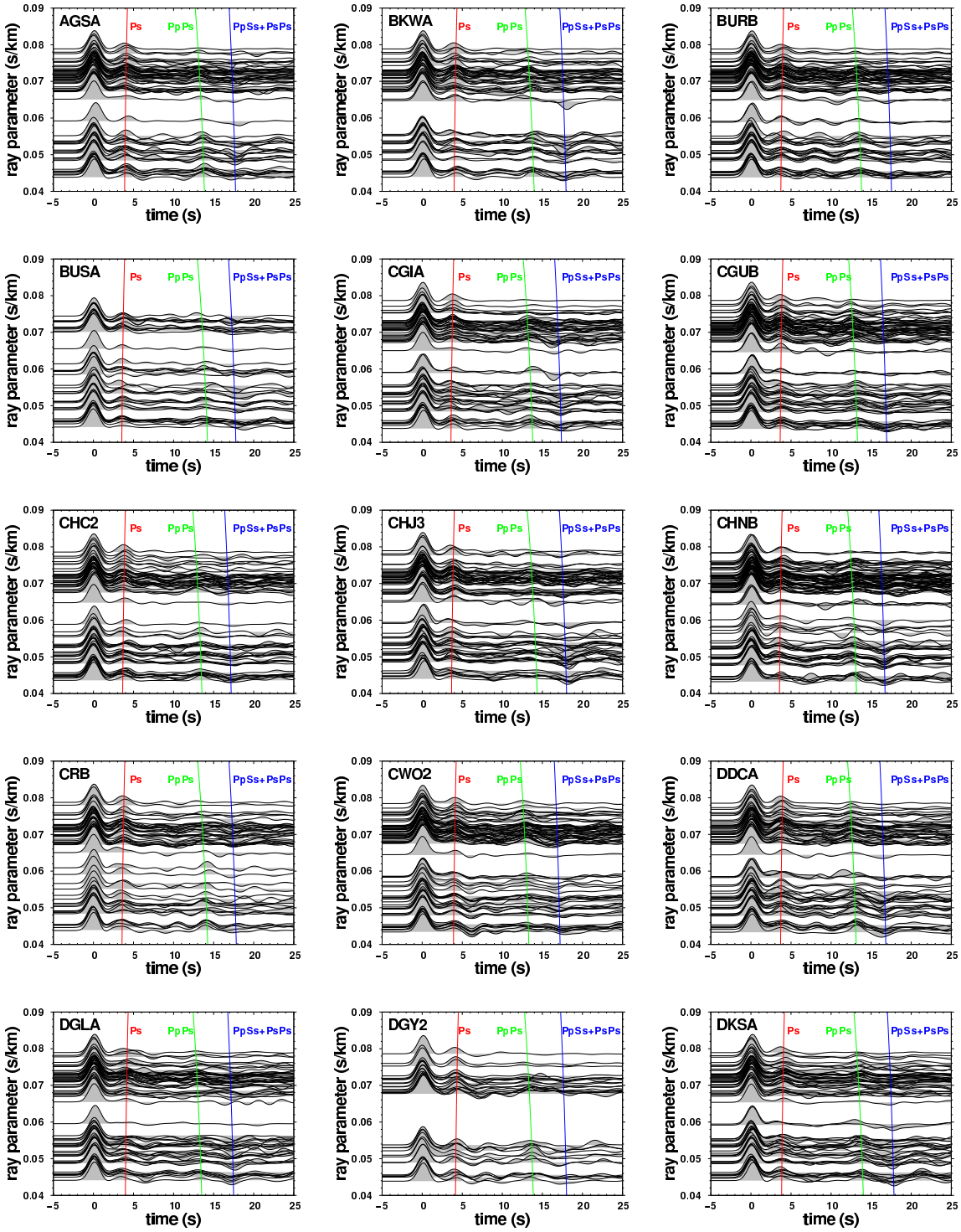

Figure S5. Receiver function profiles with Gaussian filter parameter of $\alpha = 1.0$ as a function of ray parameter. The observed receiver functions agree with the theoretical arrival times of Moho-converted phase phases (*Ps*, *PpPs*, *PsPs+PpSs*) agree with the theoretical arrival times.

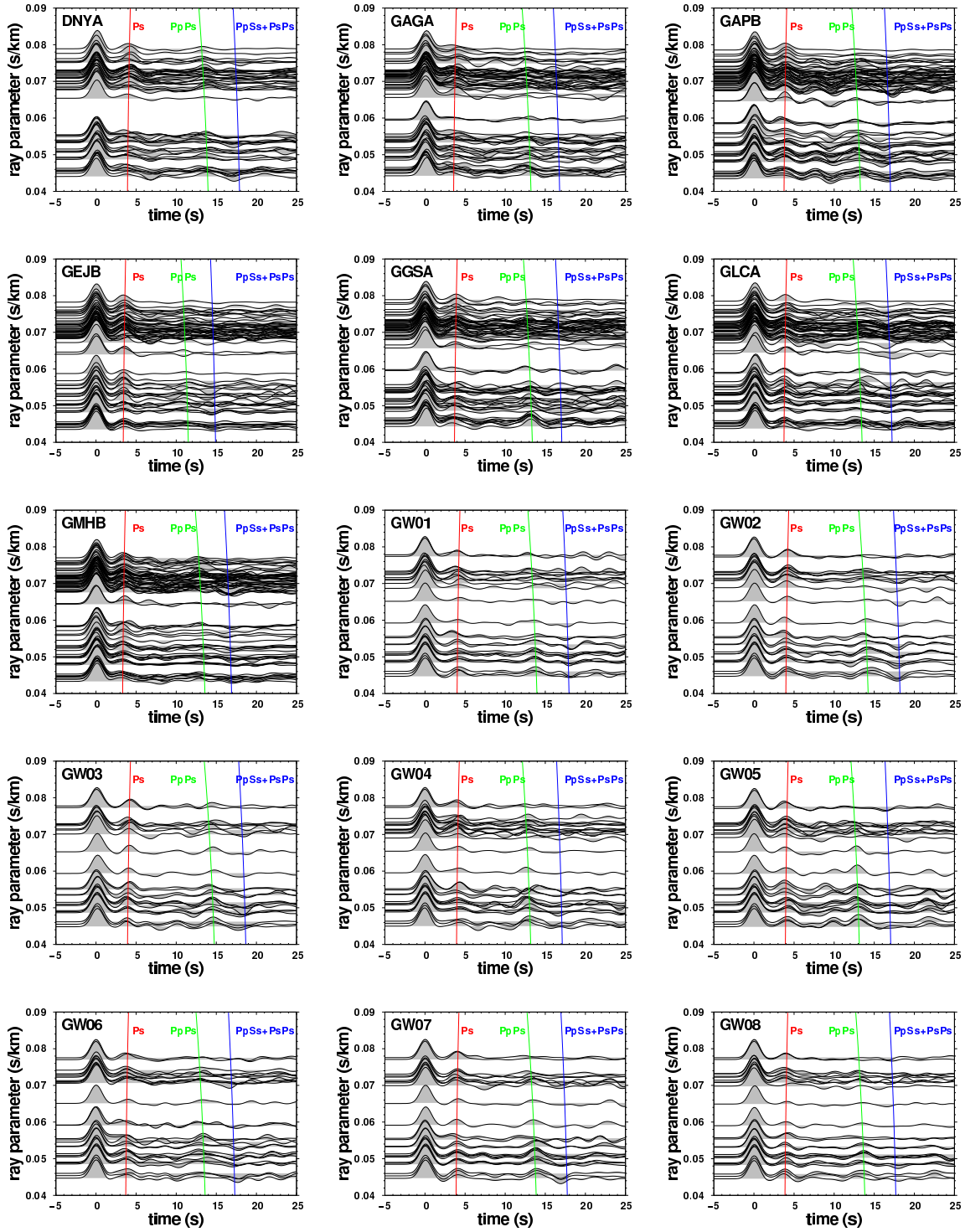

Figure S5. (*continued*)

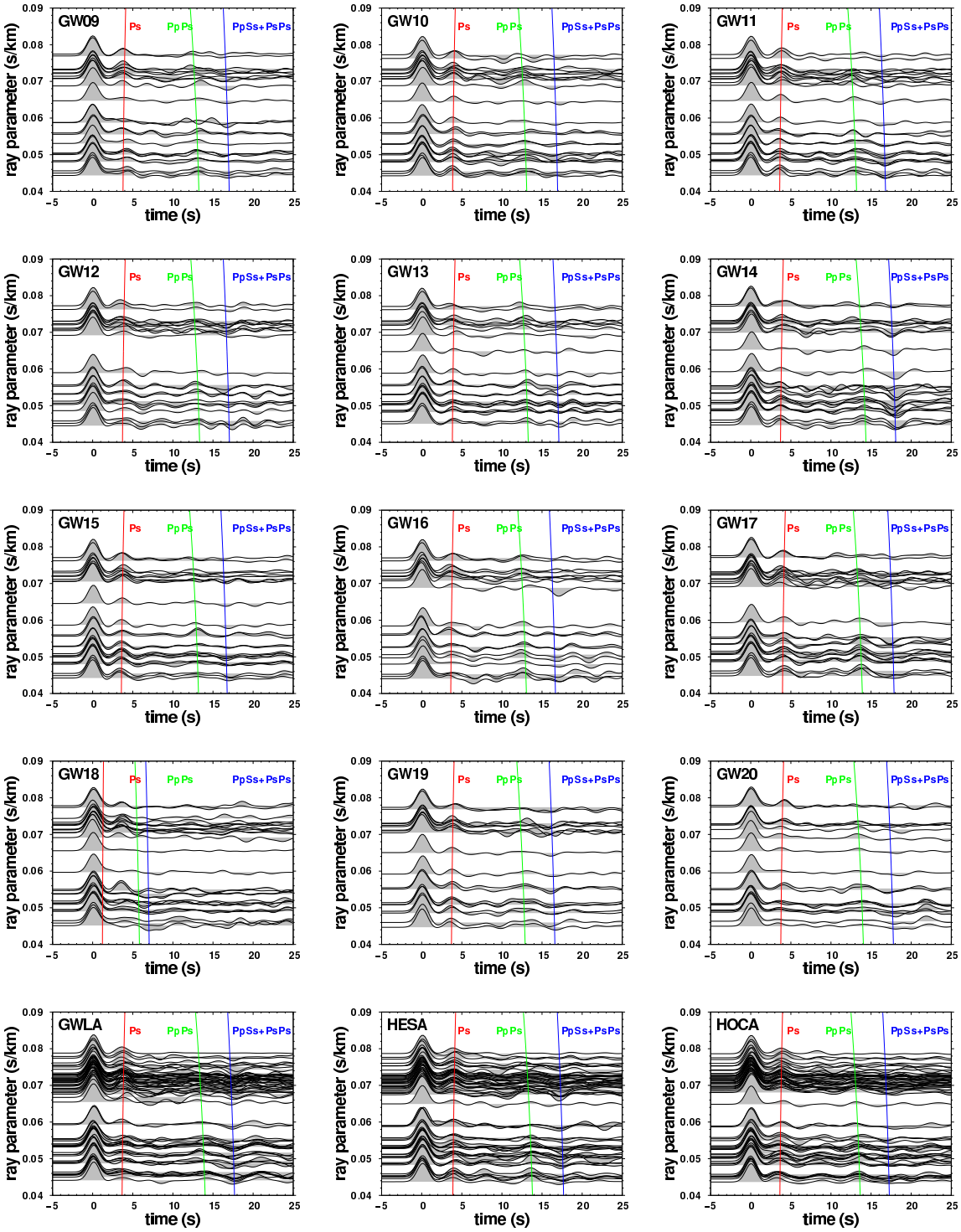

Figure S5. (*continued*)

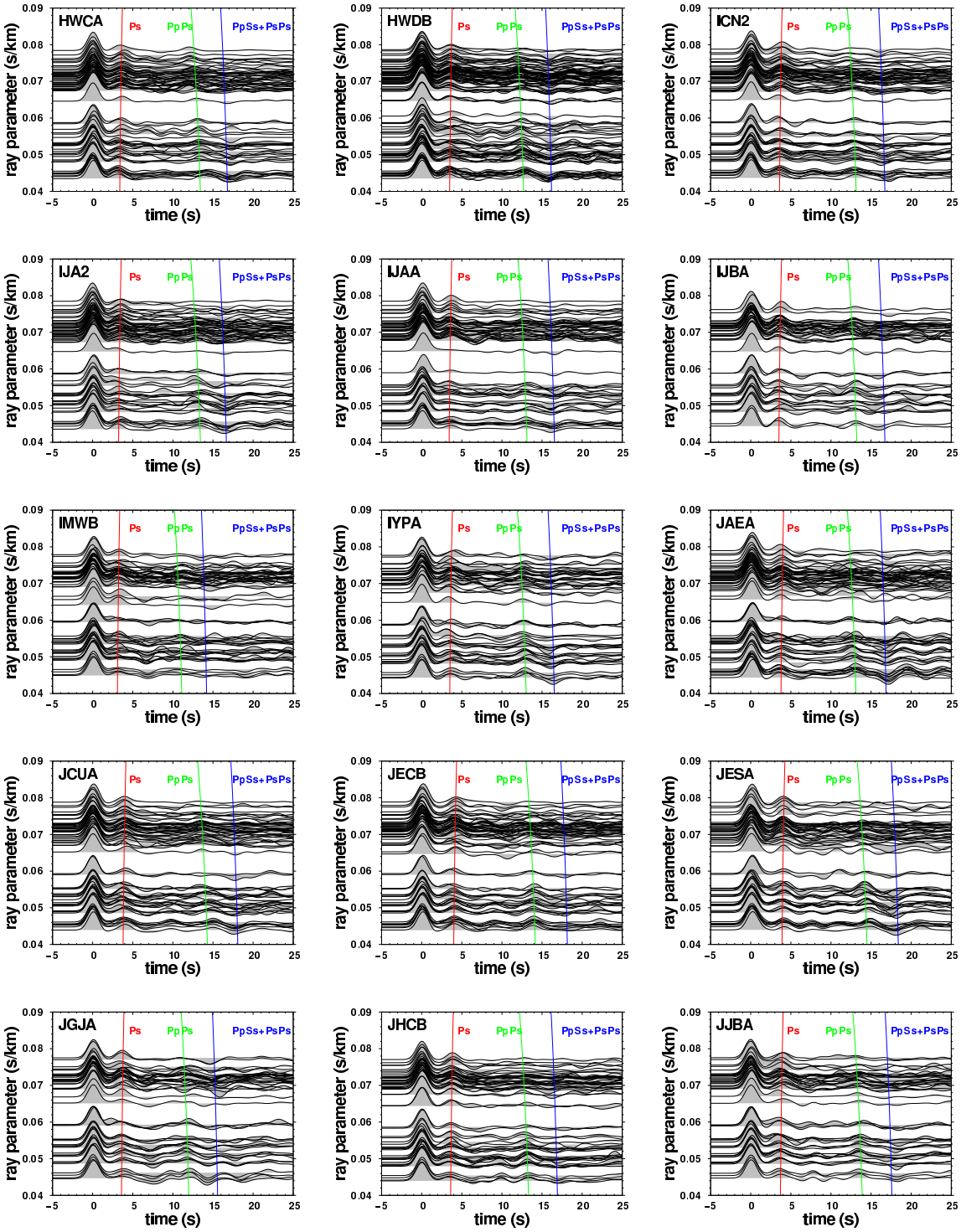

Figure S5. (*continued*)

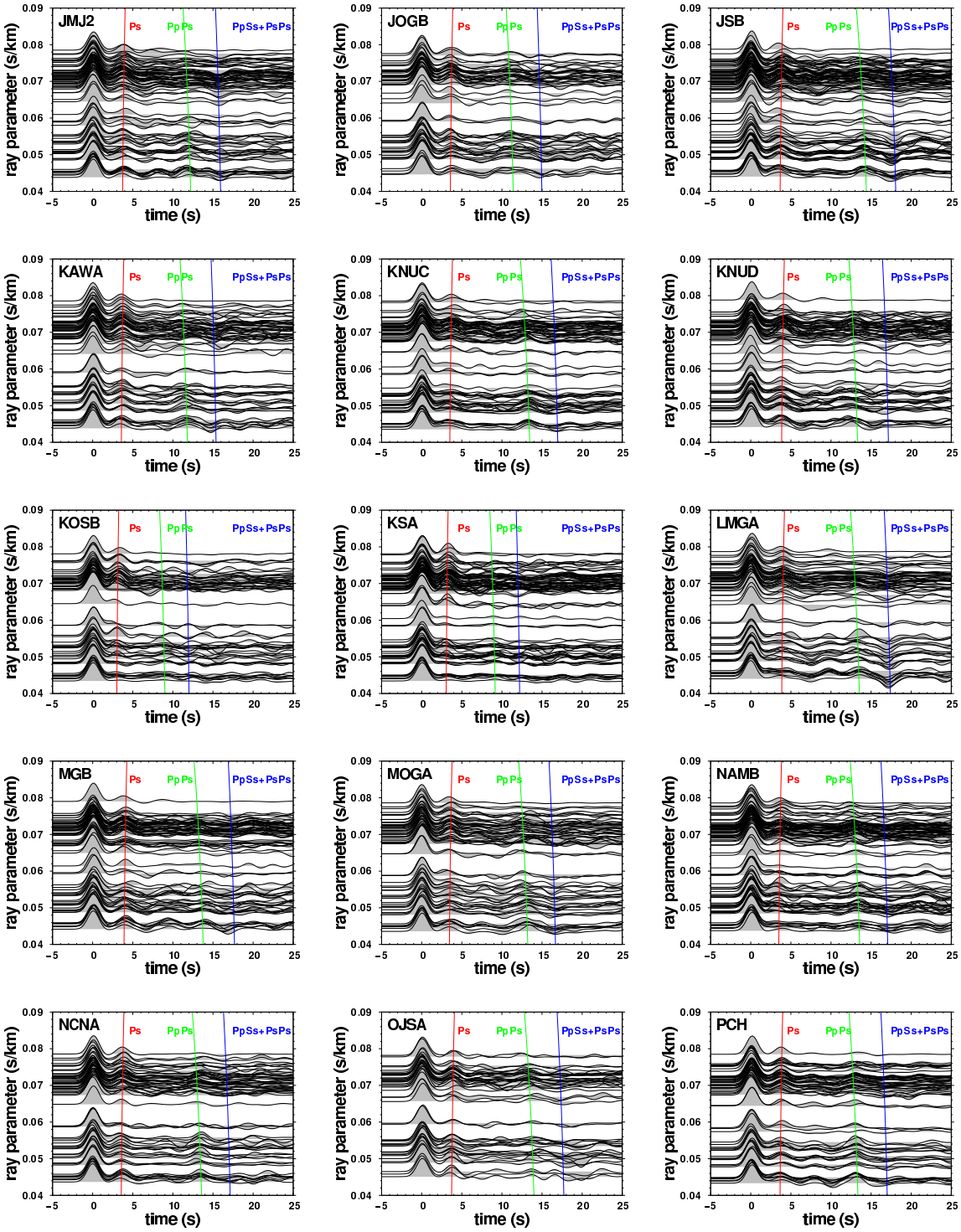

Figure S5. (*continued*)

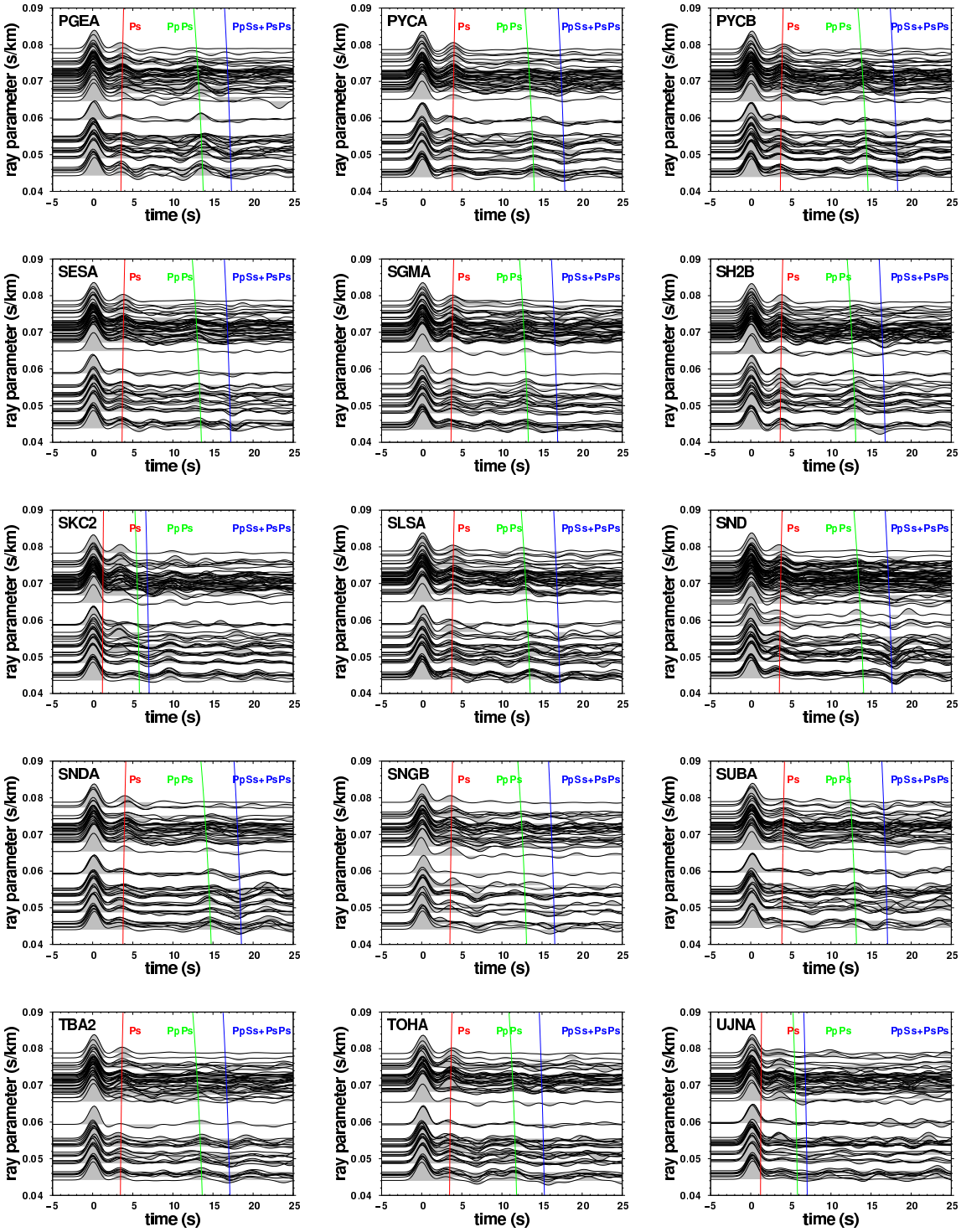

Figure S5. (*continued*)

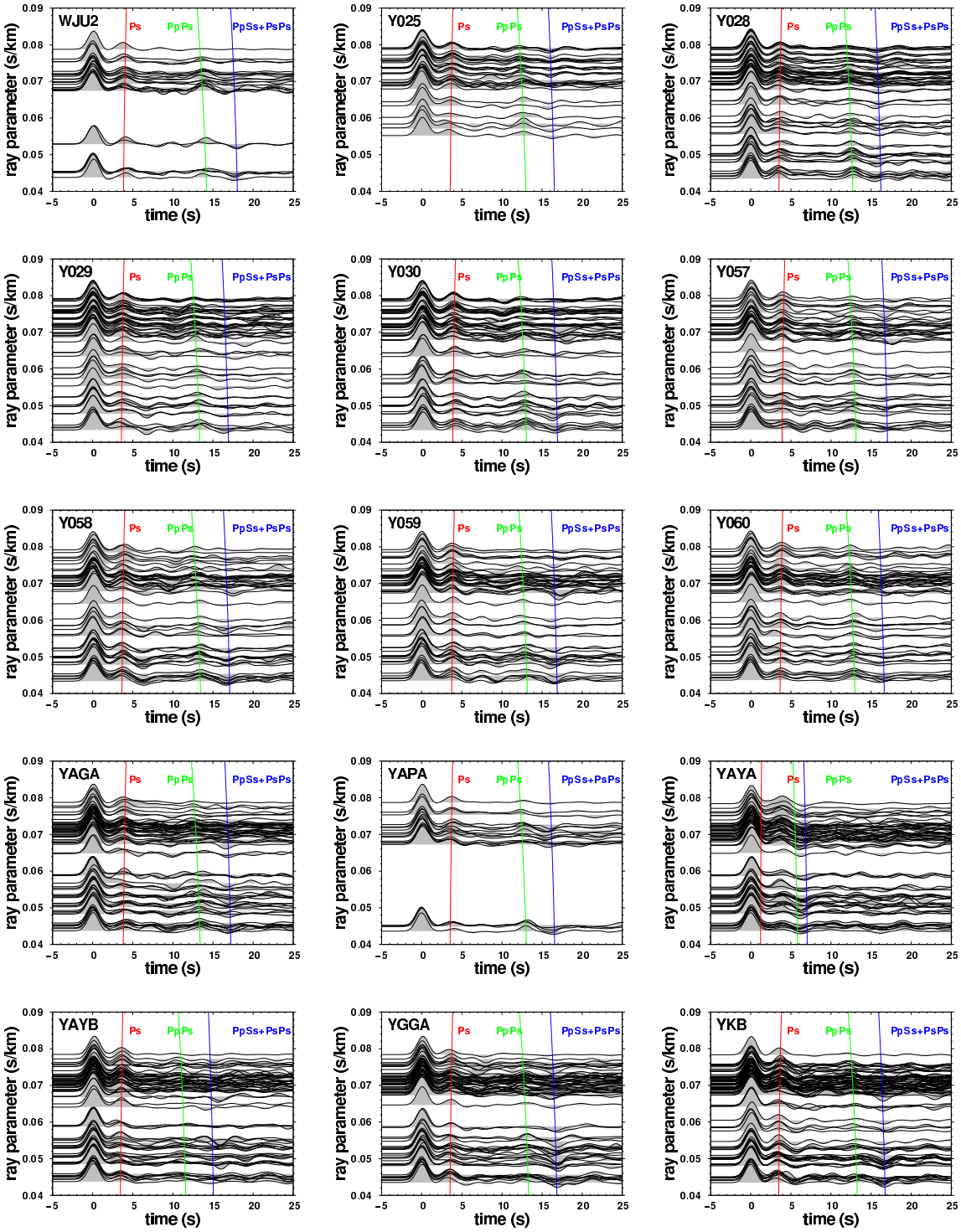

Figure S5. (*continued*)

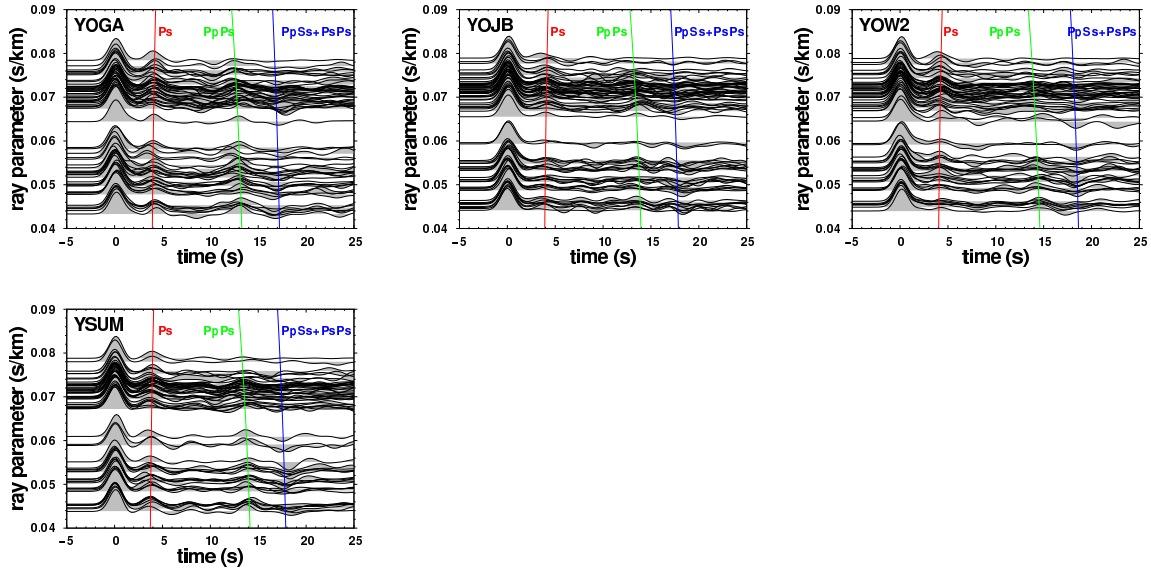

Figure S5. (*continued*)

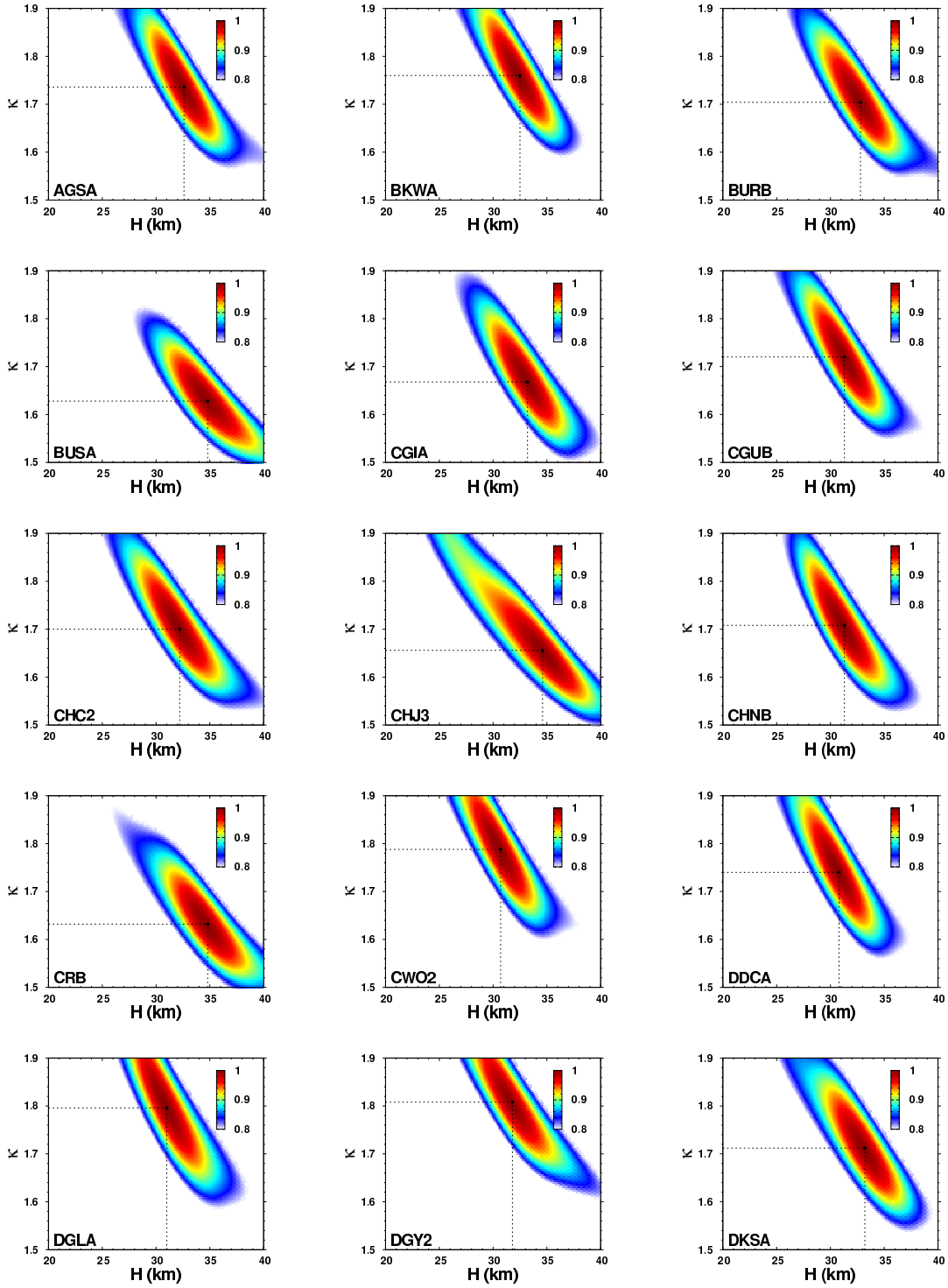

Figure S6. Example of $H - \kappa$ stacking analysis with a Gaussian filter parameter of $\alpha = 1.0$ at each station.

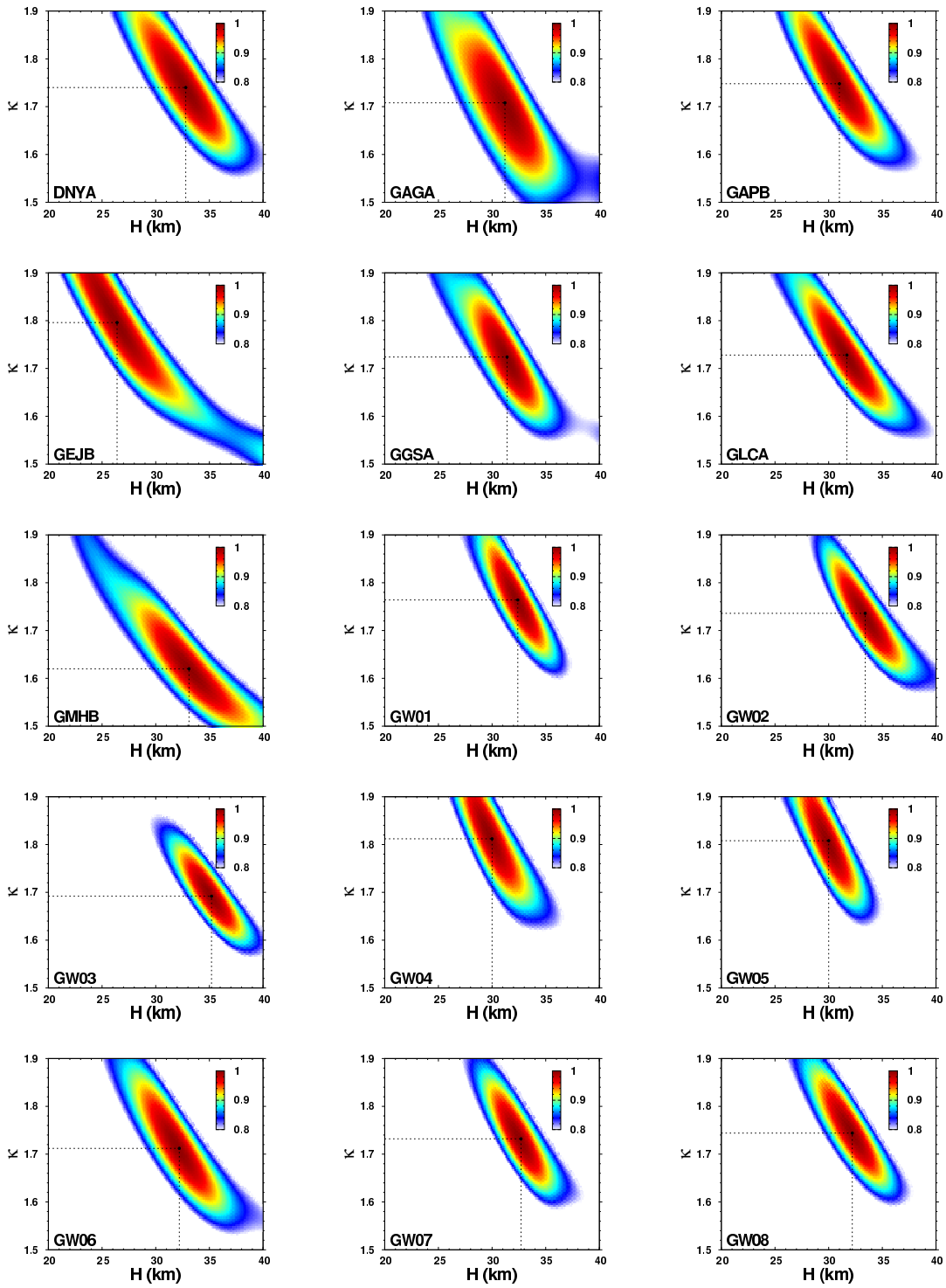

Figure S6. (*continued*)

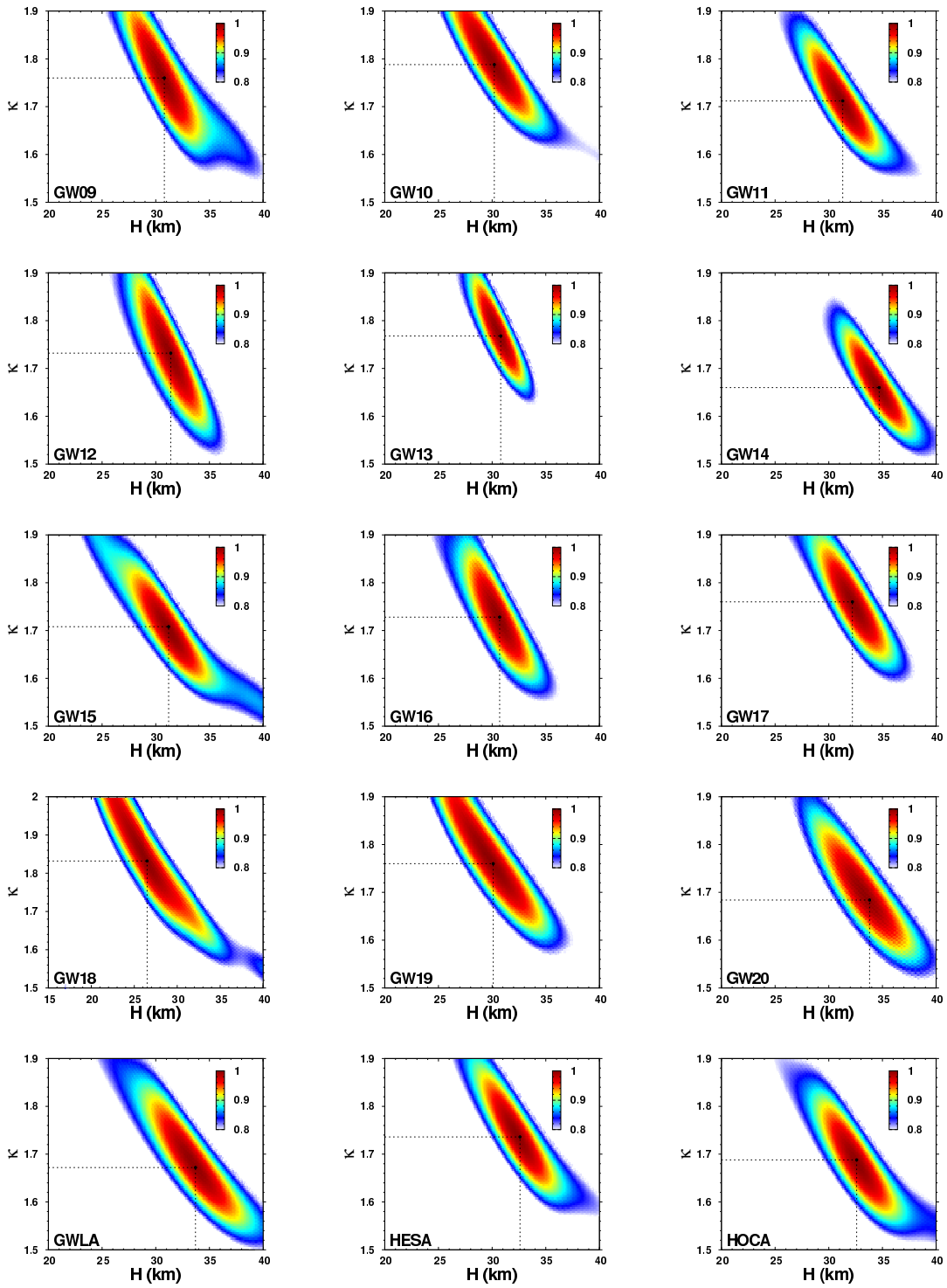

Figure S6. (*continued*)

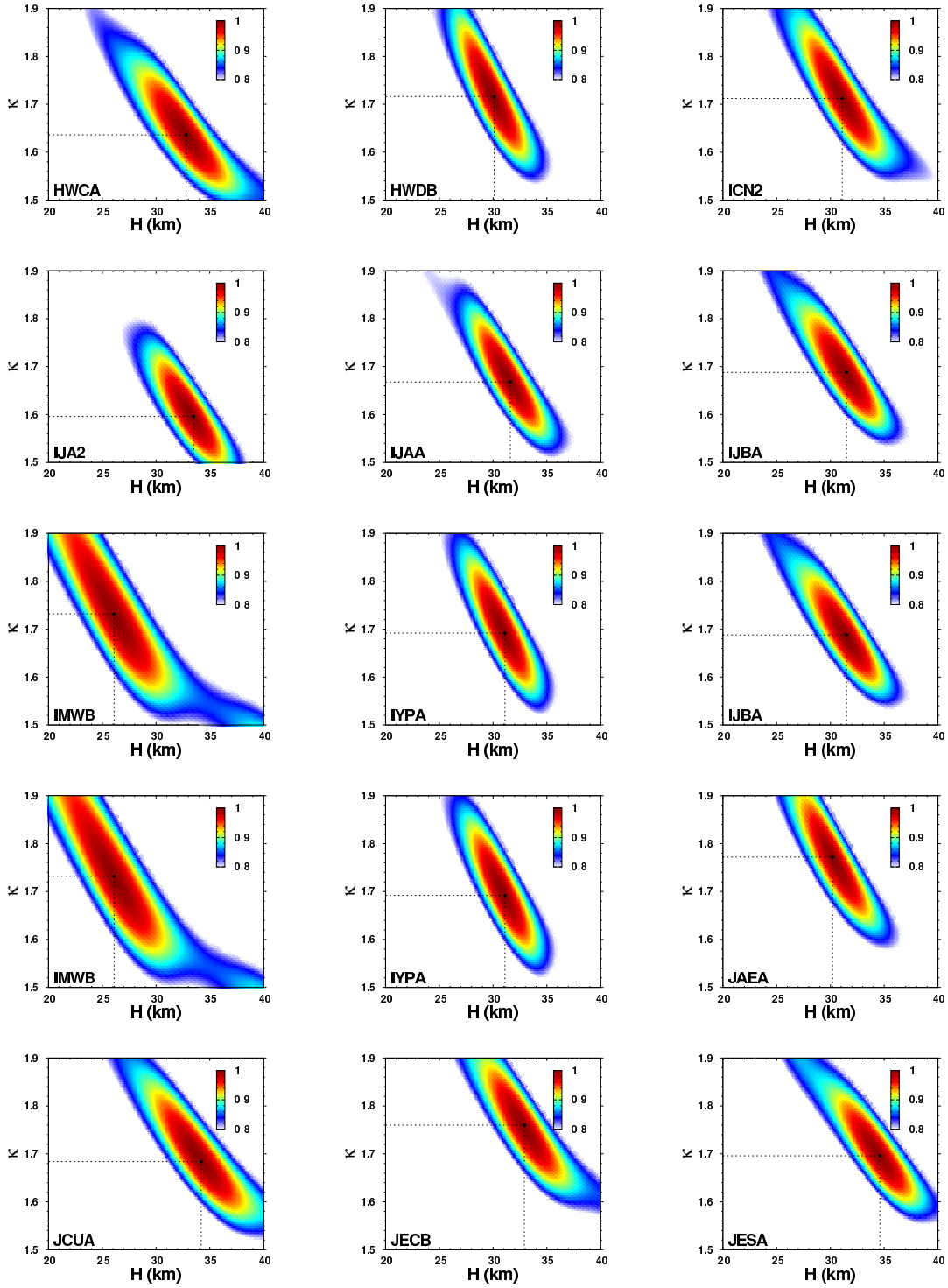

Figure S6. (*continued*)

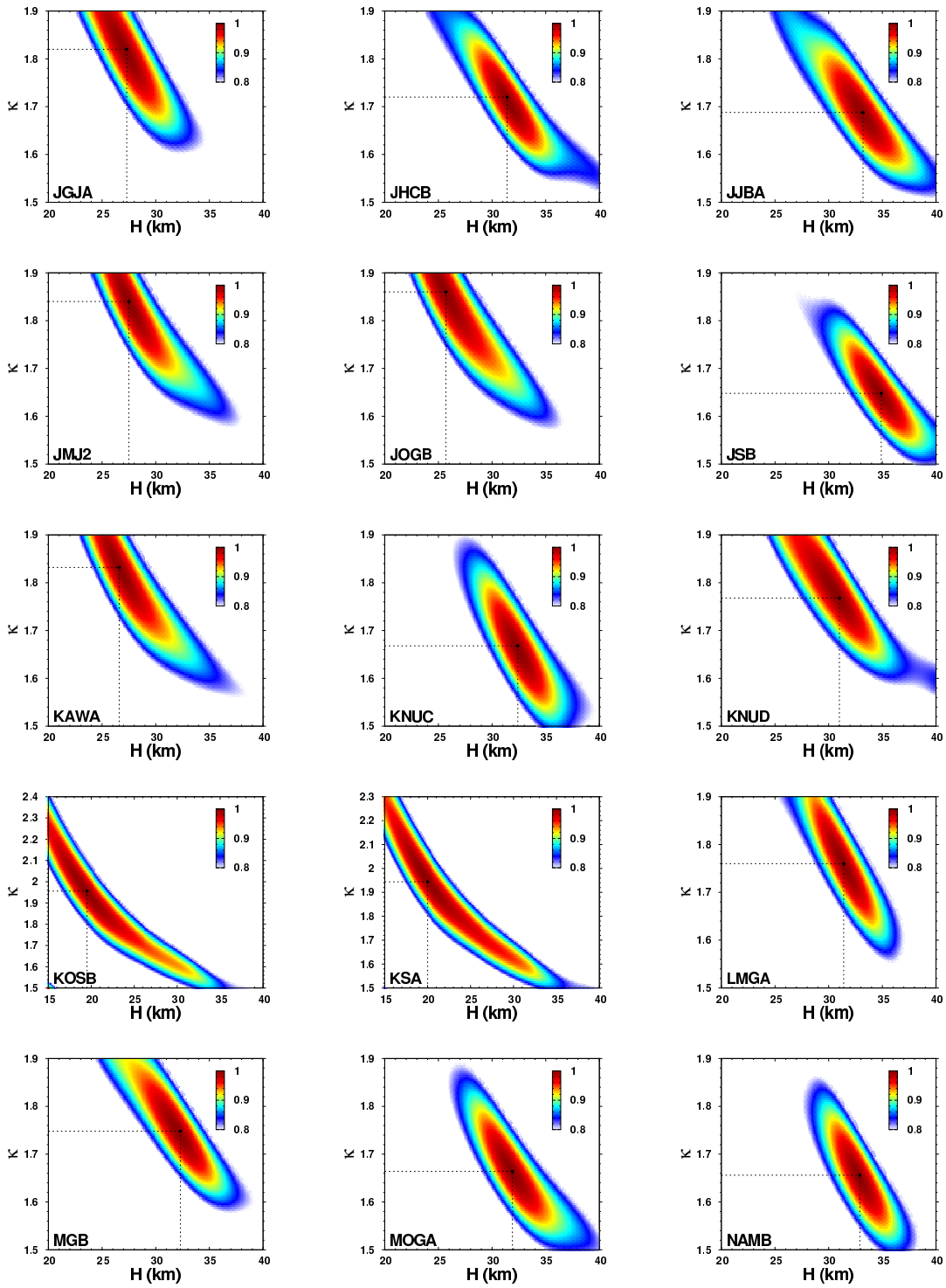

Figure S6. (*continued*)

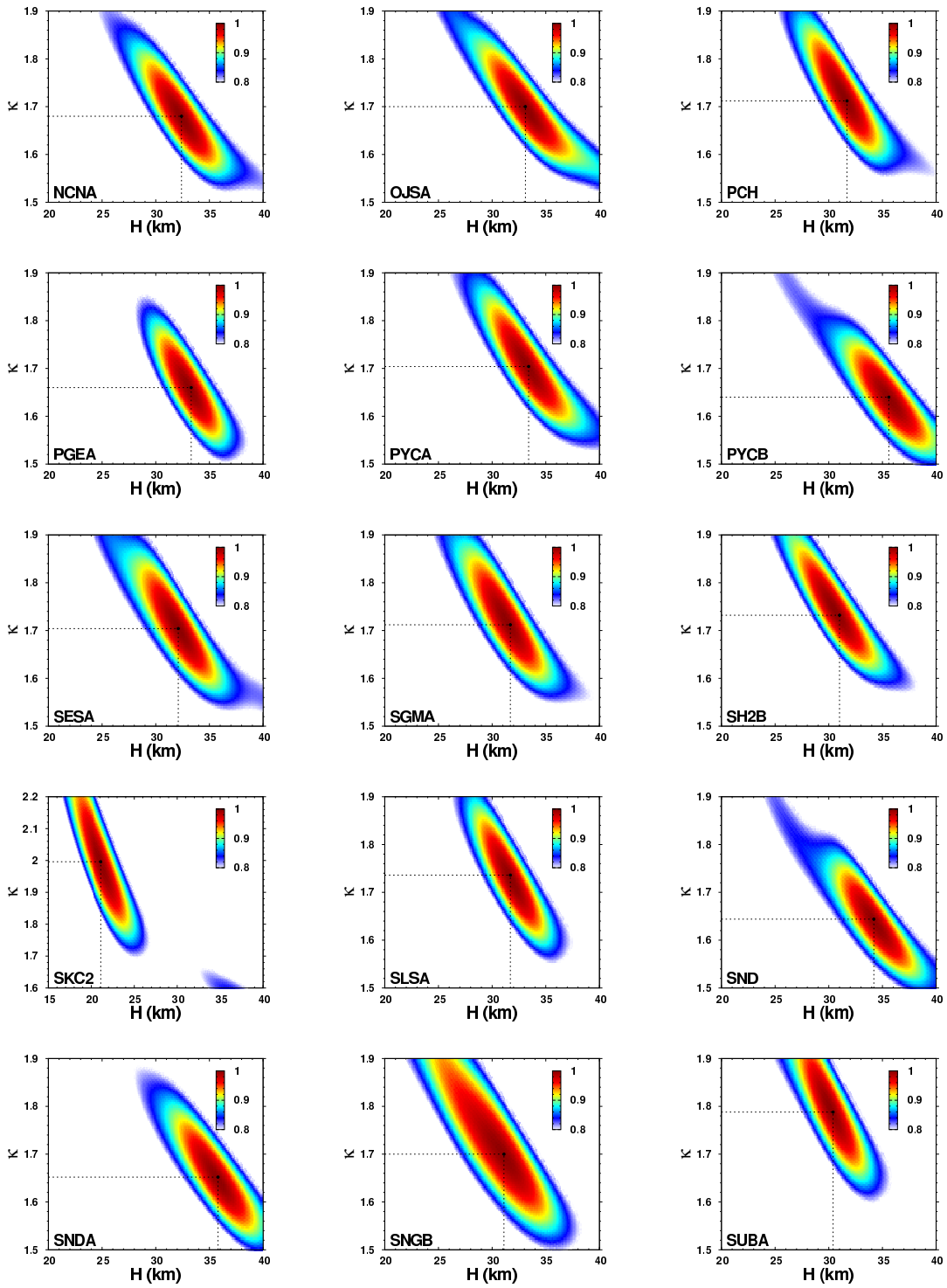

Figure S6. (*continued*)

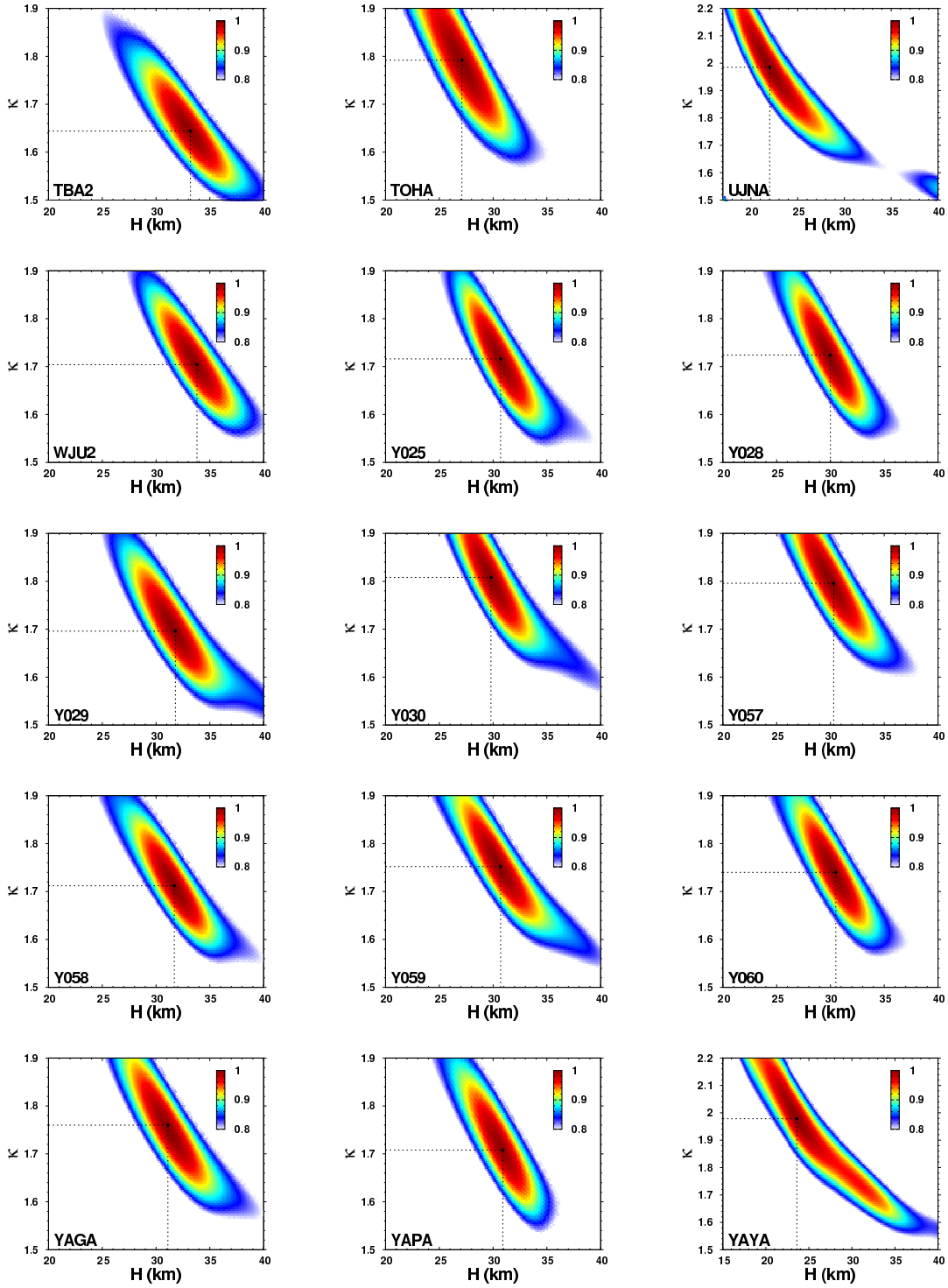

Figure S6. (*continued*)

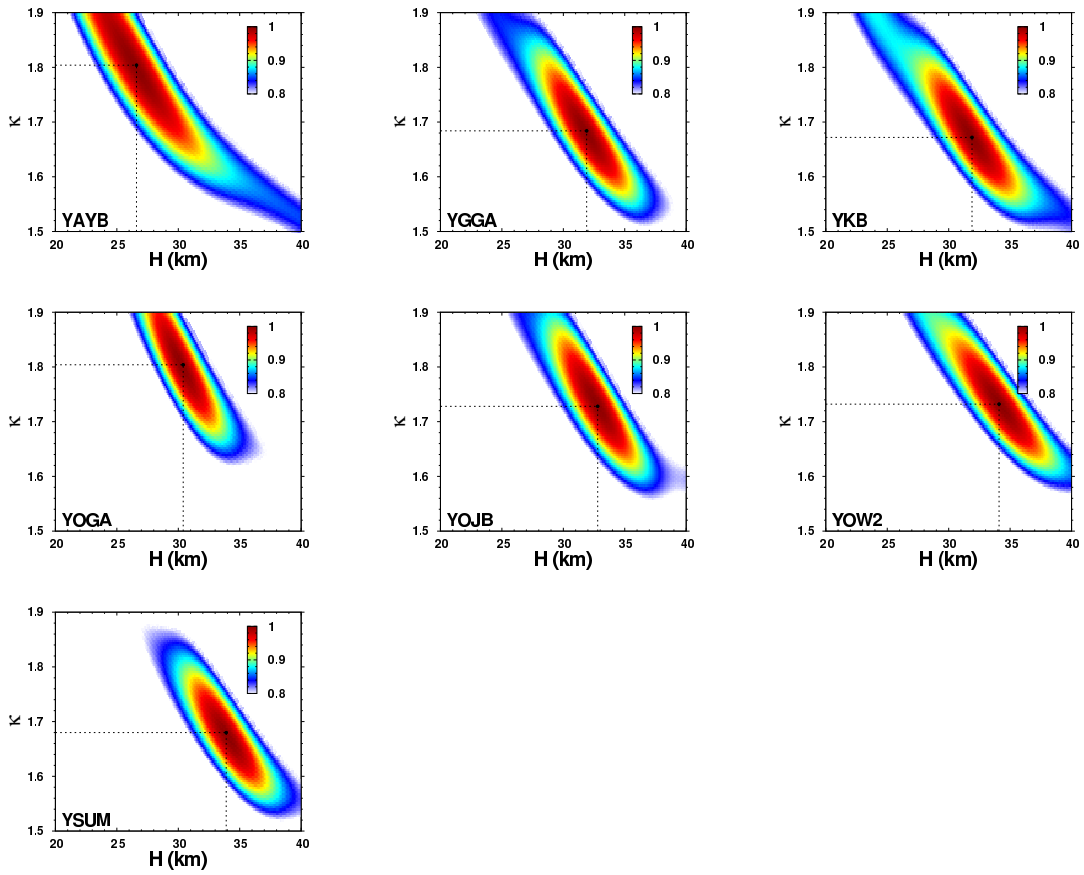

Figure S6. (*continued*)

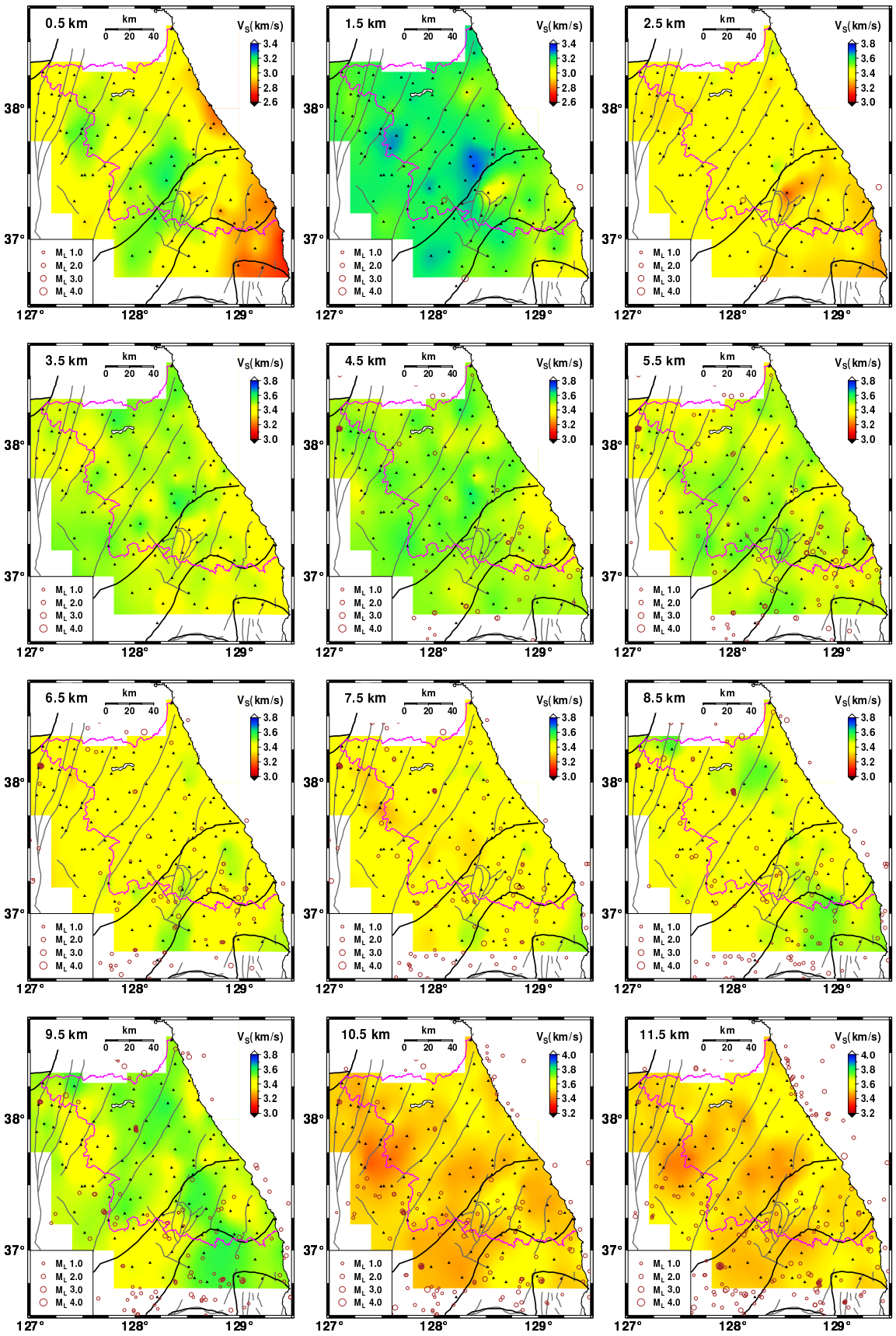

Figure S7. Shear-wave velocity models from joint inversion analysis with an influence factor of 0.15 at depths of 0.5-39.5 km. Fault traces and geological boundaries (solid lines) are presented. Earthquakes at the depths (circles) are marked. The shear-wave velocities change laterally.

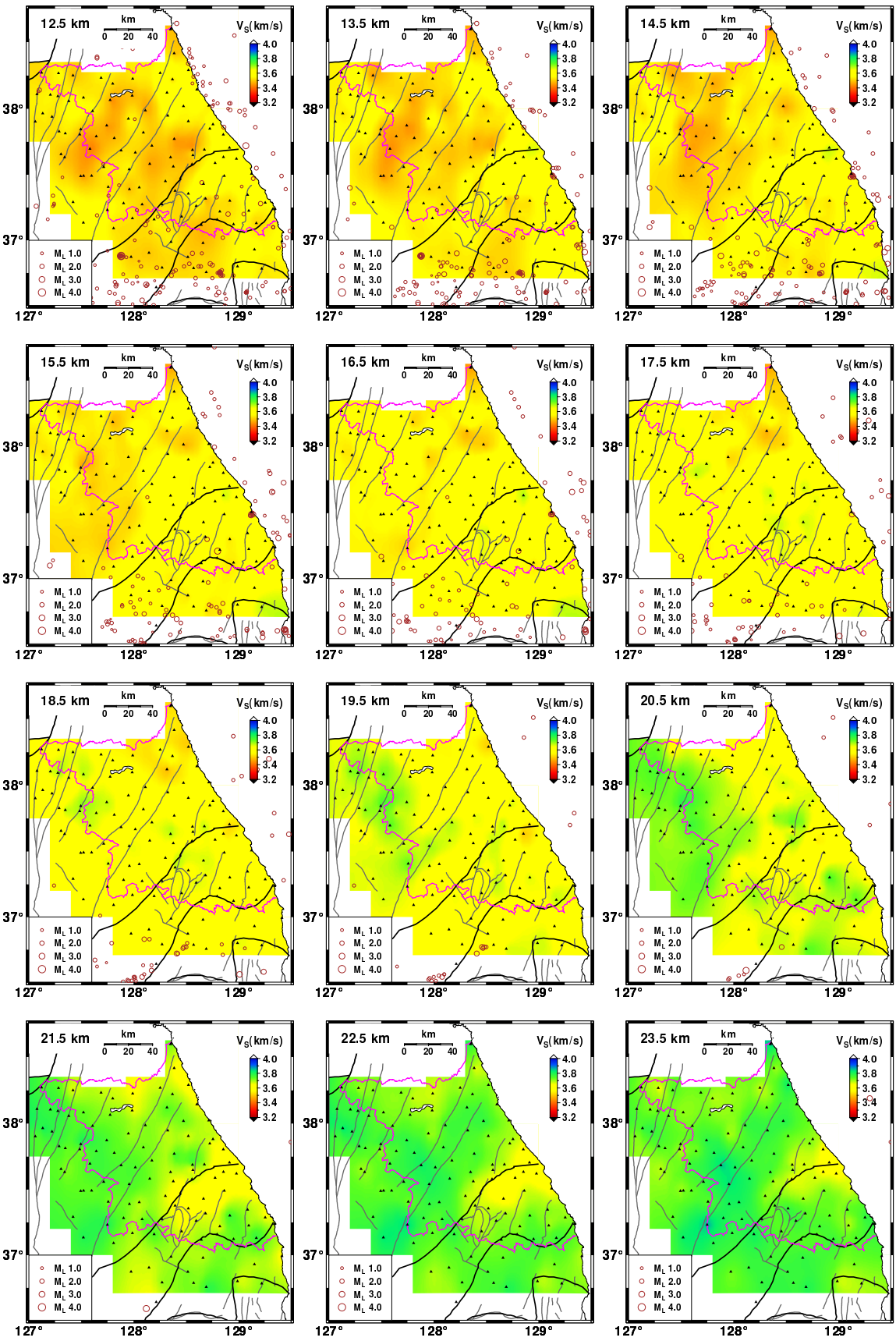

Figure S7. (*continued*)

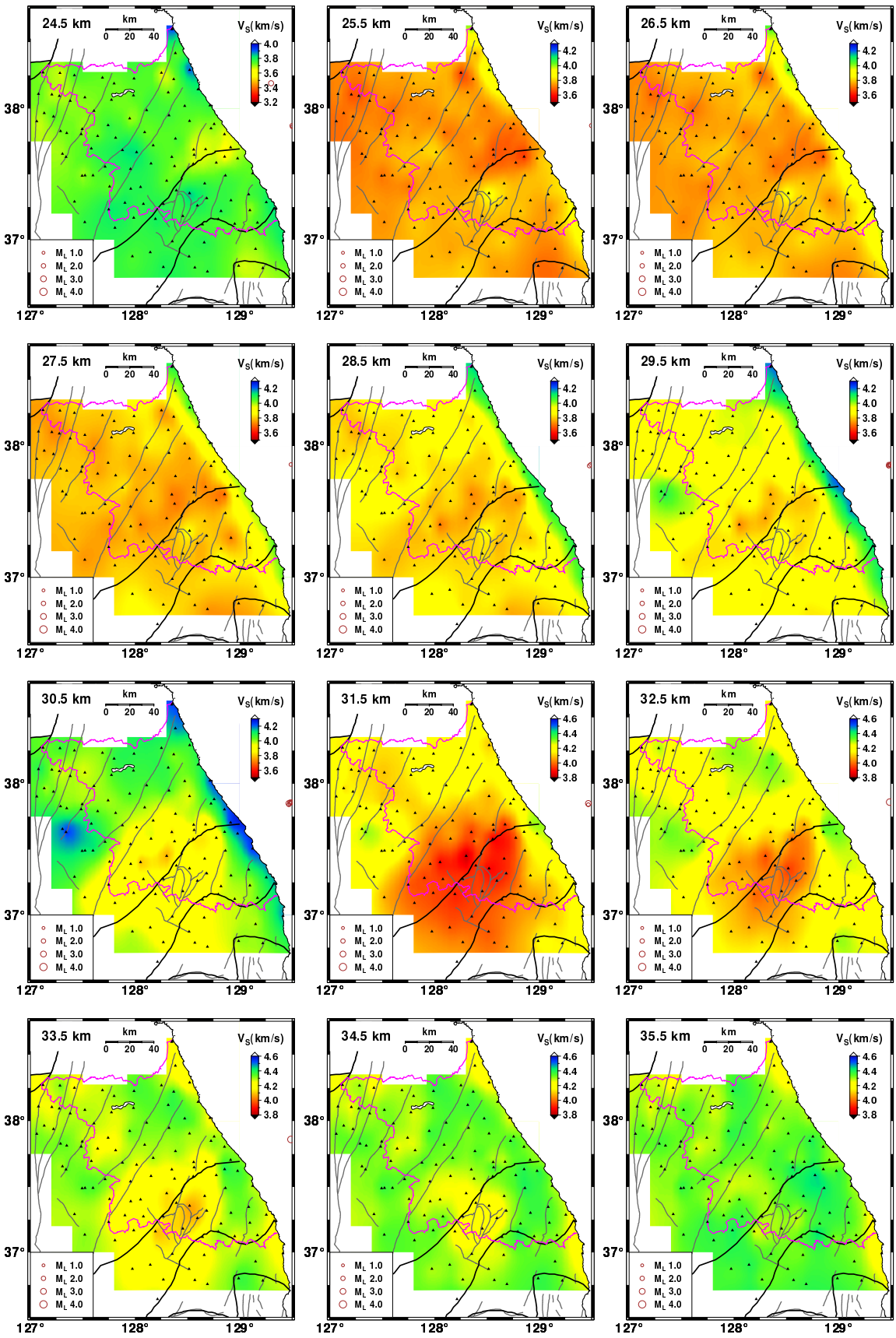

Figure S7. (*continued*)

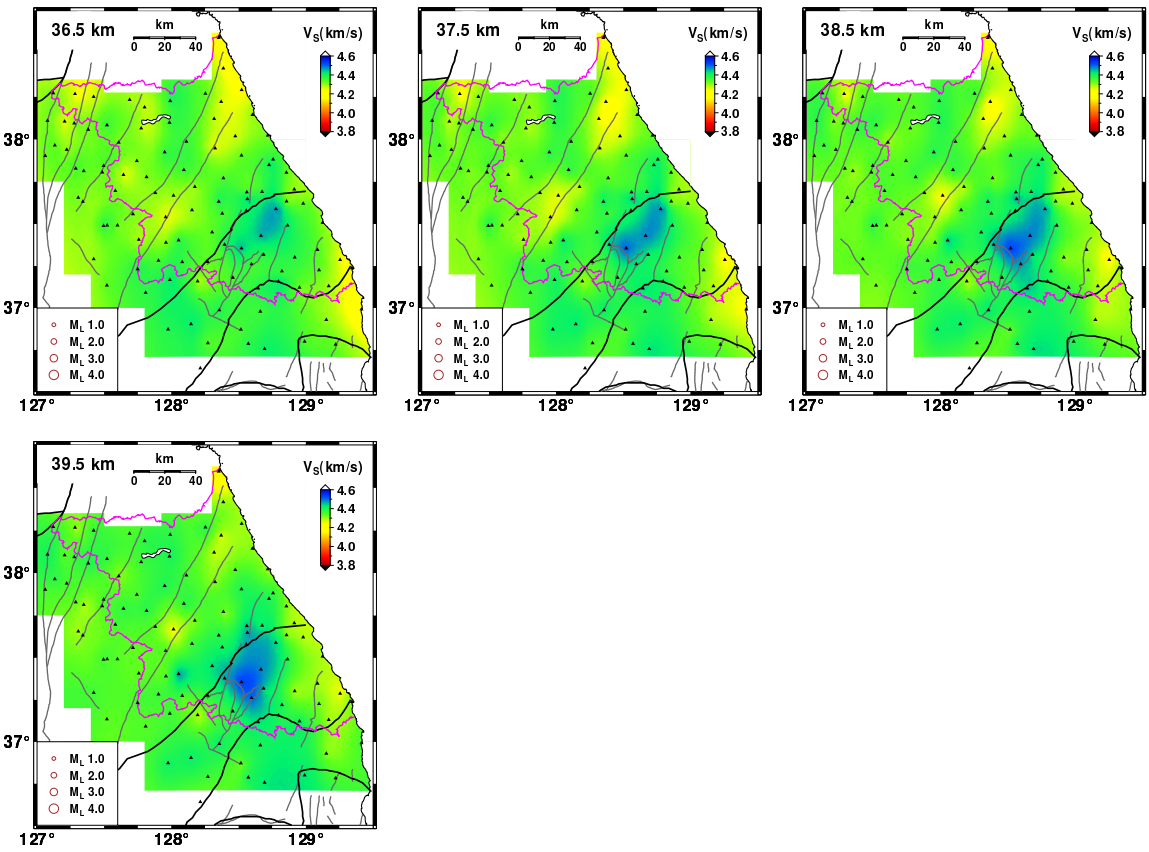

Figure S7. (*continued*)

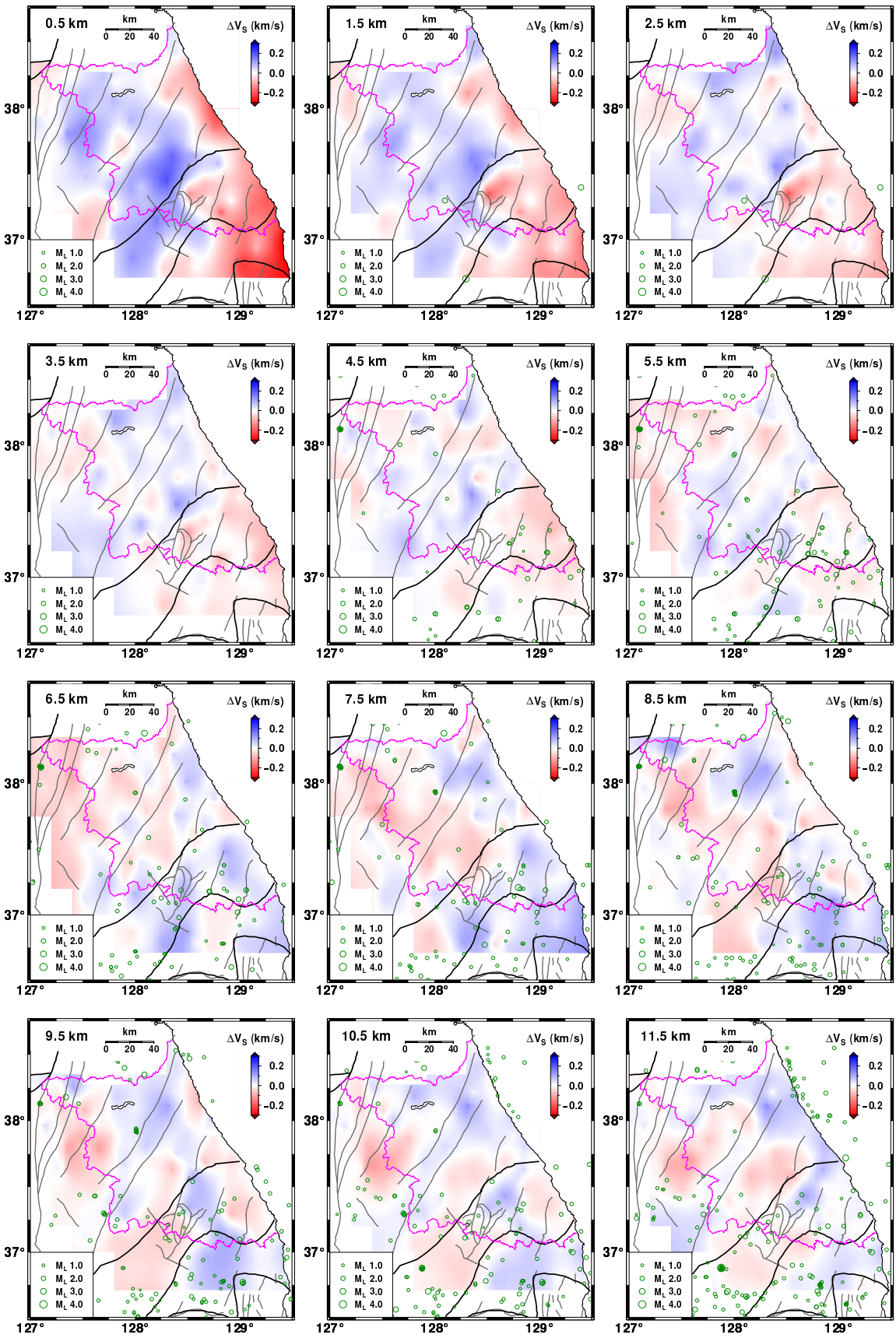

Figure S8. Differential shear-wave velocity models from joint inversion analysis with an influence factor of 0.15 at depths of 0.5-39.5 km. Fault traces and geological boundaries (solid lines) are presented. Earthquakes at the depths (circles) are marked.

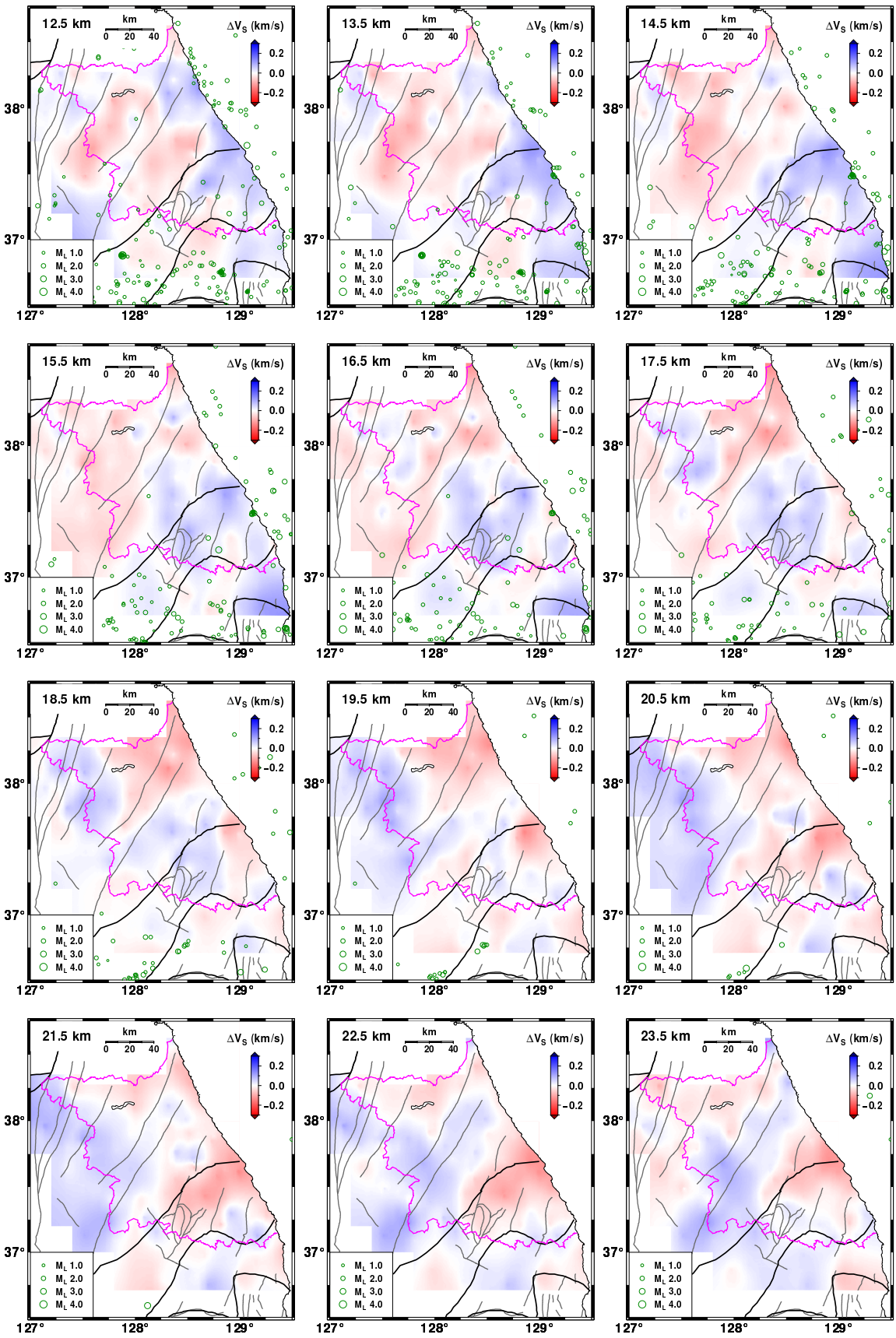

Figure S8. (*continued*)

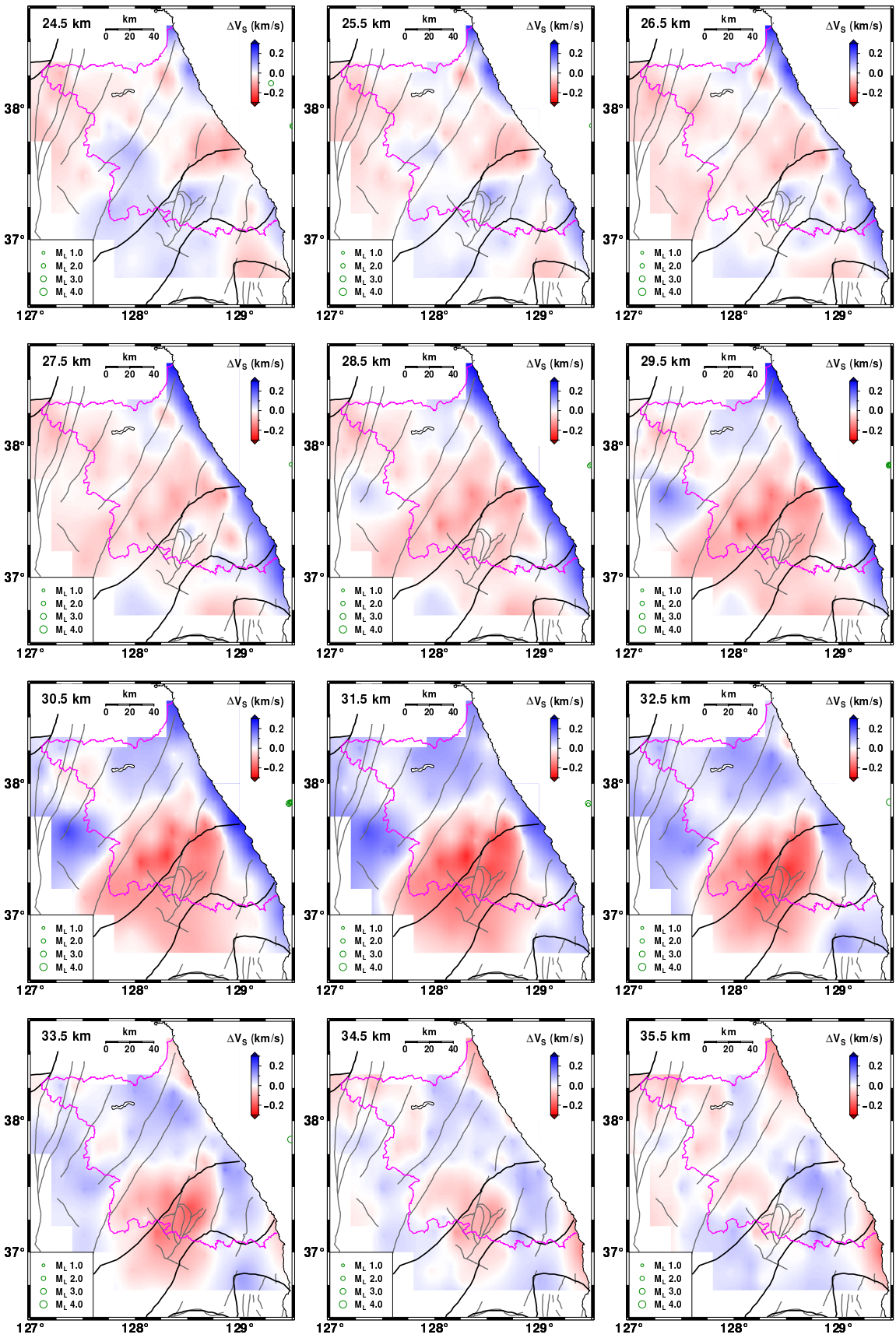

Figure S8. (*continued*)

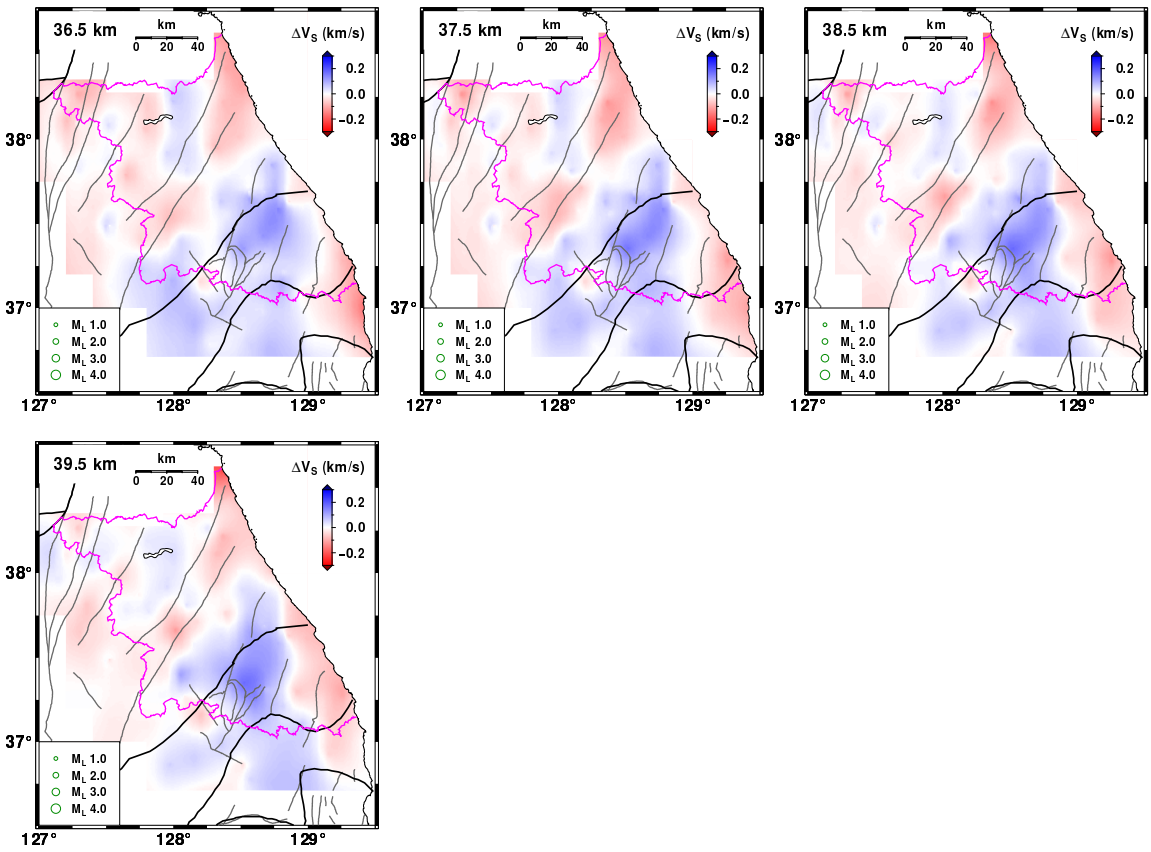

Figure S8. (*continued*)

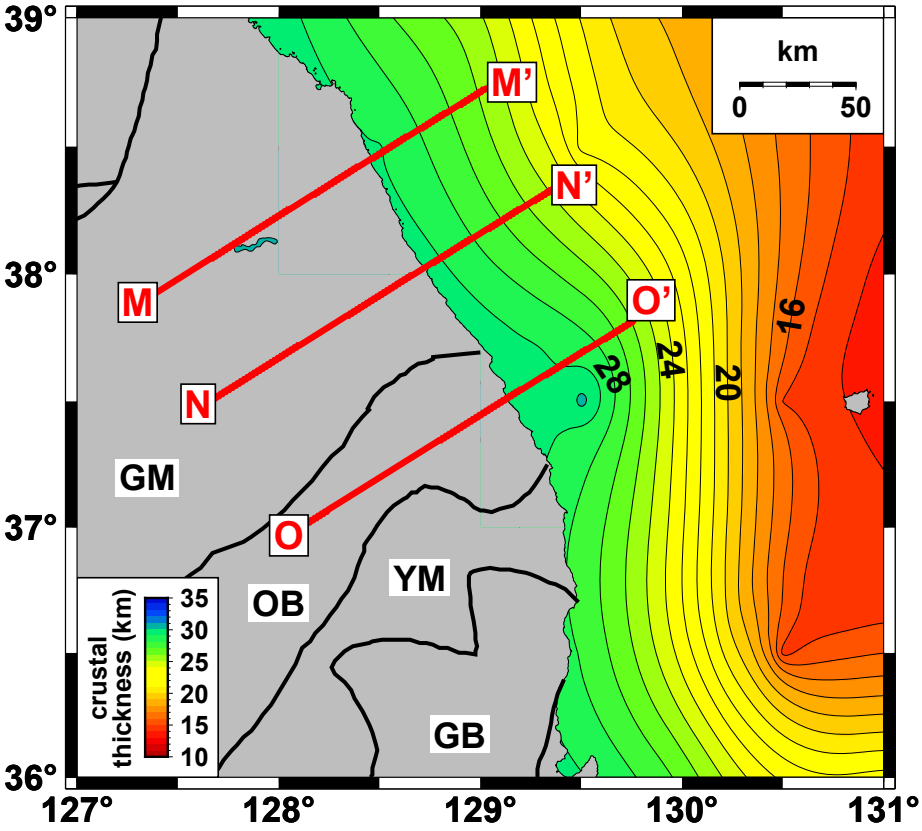

Figure S9. Map of crustal thickness from CRUST1.0 (Laske et al., 2013). The crustal thicknesses in the East Sea are presented using interpolation. Three profiles across the coast are marked (MM', NN', and OO').

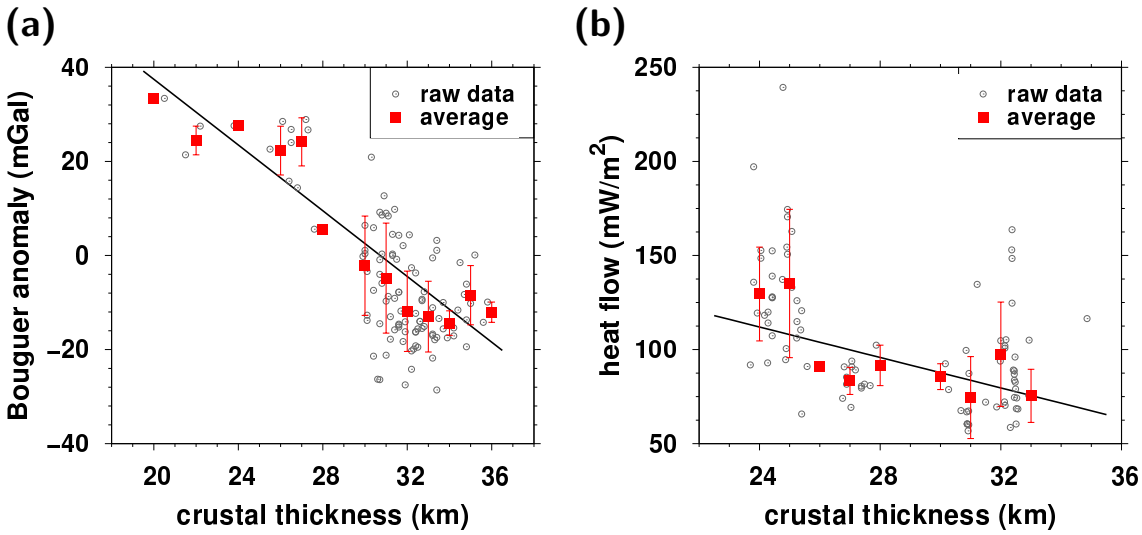

Figure S10. Comparisons (a) between Bouguer gravity anomalies and crustal thicknesses, and (b) between heat flows and crustal thicknesses, presenting apparent negative linear relationships.

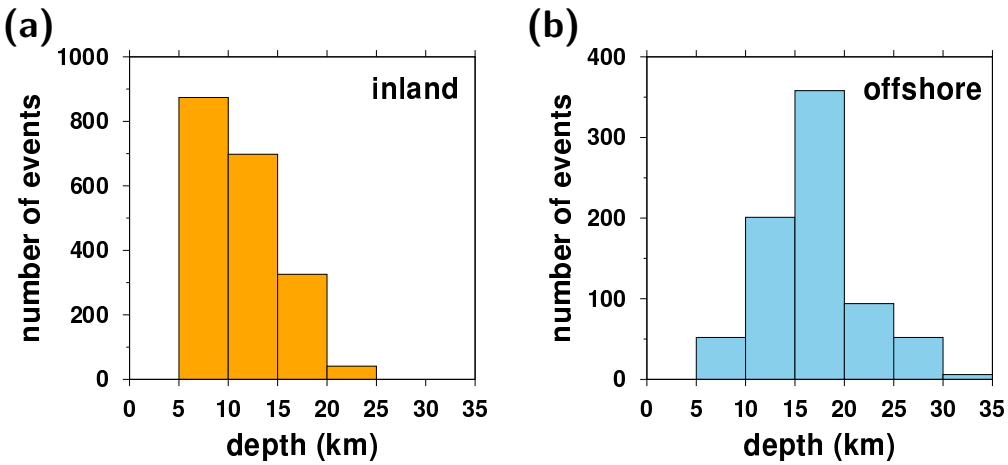

Figure S11. Focal-depth distribution of (a) inland and (b) offshore earthquakes in January 2010 to July 2025 reported by the Korea Meteorological Administration (KMA).

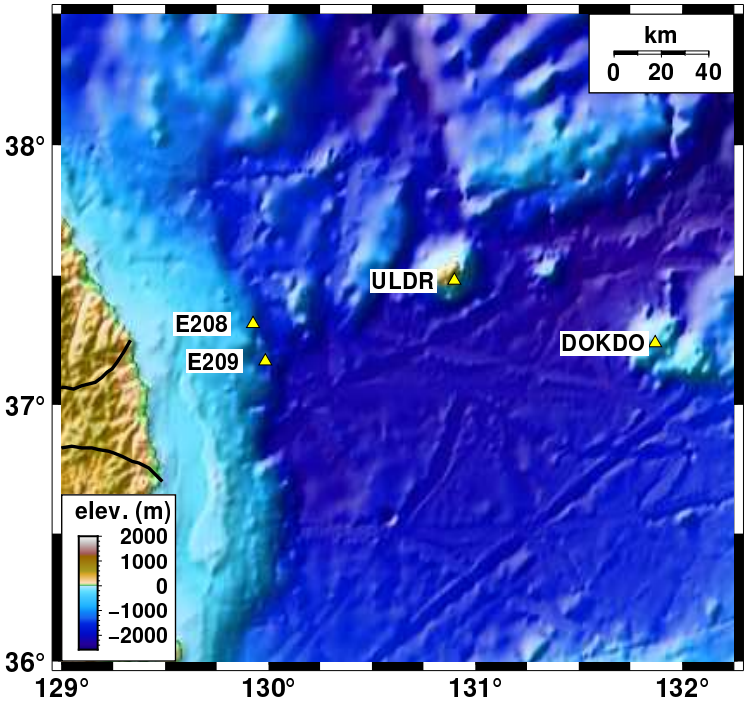

Figure S12. Map of offshore stations. Two island stations (ULDR and DOKDO) and two OBS stations (E208 and E209) are considered. The OBS stations are located in the boundary between Hupo bank and Ulleung basin.

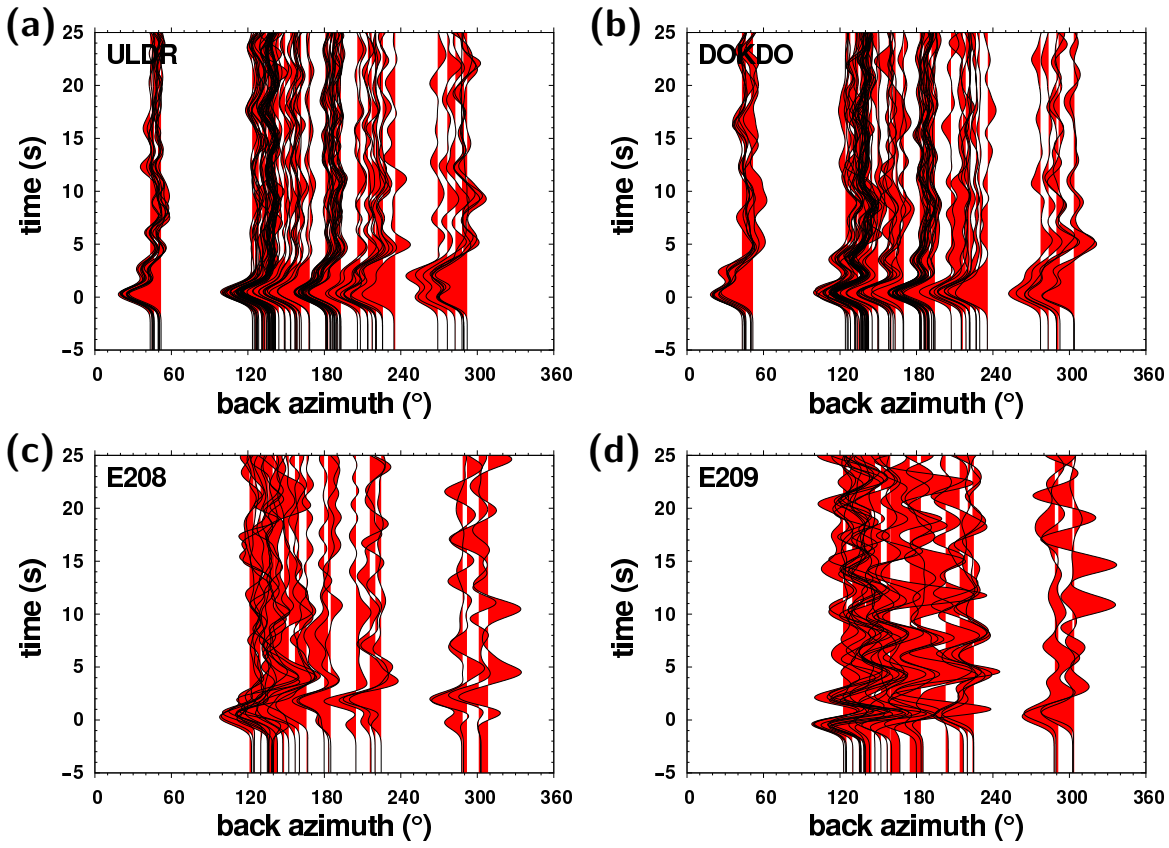

Figure S13. Receiver function profiles for offshore stations (a) ULDR, (b) DOKDO, (c) E208, and (d) E209 as a function of backazimuth. Gaussian filter parameter of $\alpha = 1.0$ is applied.

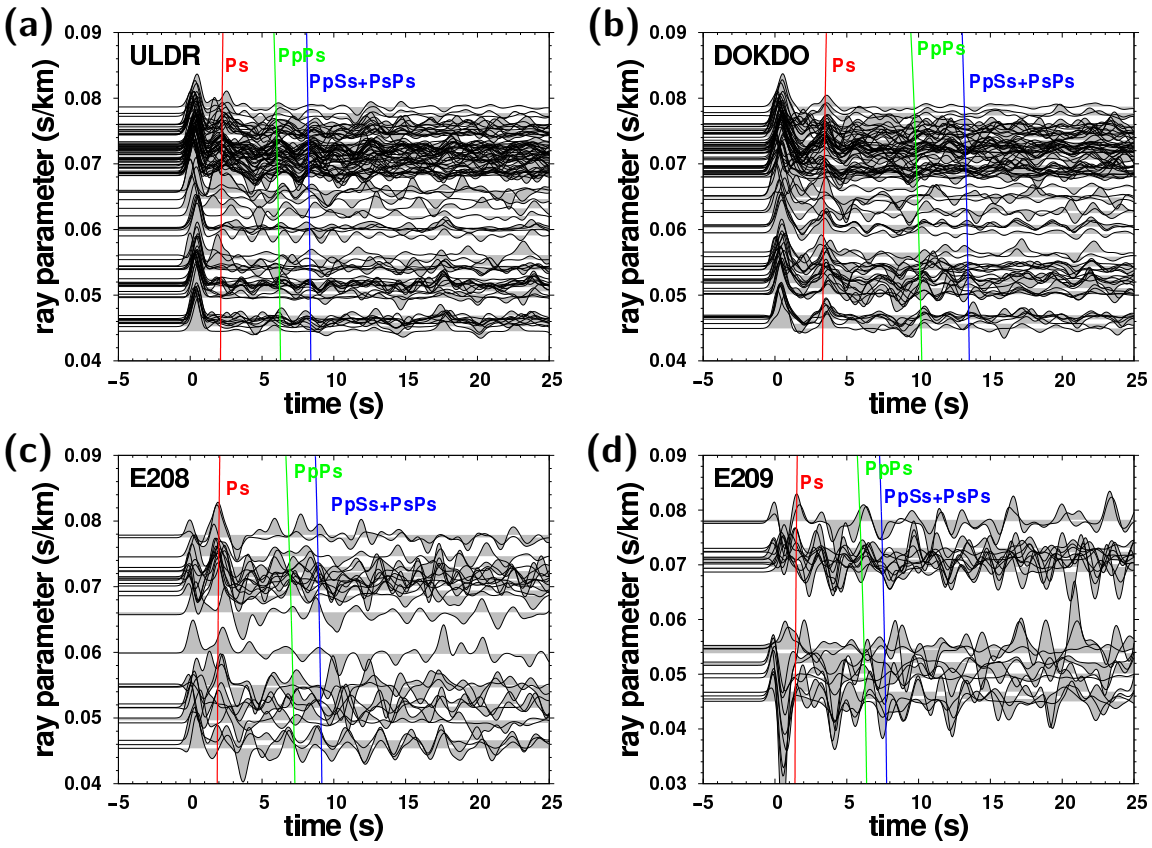

Figure S14. Receiver function profiles with Gaussian filter parameter of $\alpha = 2.5$ as a function of ray parameter at offshore stations (a) ULDR, (b) DOKDO, (c) E208, and (d) E209. The Moho-converted phase arrival times are indicated.

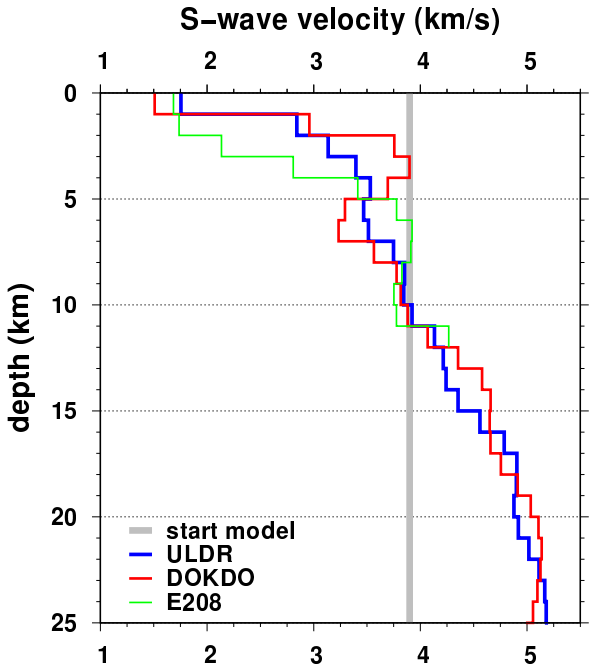

Figure S15. Shear-wave velocity models of the media beneath offshore stations.